INSTITUTO DE PESQUISAS ENERGÉTICAS E NUCLEARES
Autarquia Associada à Universidade de São Paulo

Study of cirrus clouds physical properties over the state of São Paulo, Brazil, from CALIPSO/CALIOP level 2 data

GIOVANNI SOUZA

Dissertação apresentada como parte dos requisitos para obtenção do Grau de Mestre em Ciências na Área de Tecnologia Nuclear - Materiais

Orientador:
Prof. Dr. **Eduardo Landulfo**

São Paulo
2023

INSTITUTO DE PESQUISAS ENERGÉTICAS E NUCLEARES

Autarquia associada à Universidade de São Paulo

Study of cirrus clouds physical properties over the state of São Paulo, Brazil, from CALIPSO/CALIOP level 2 data

Versão Corrigida
Versão Original disponível no IPEN

GIOVANNI SOUZA

Dissertação apresentada como parte dos requisitos para obtenção do Grau de Mestre em Ciências na Área de Tecnologia Nuclear – Materiais;

Supervisor: Prof. Dr. Eduardo Landulfo

SÃO PAULO
2023

Fonte de Financiamento: CAPES Processo n. 88887.506522/2020-00

Como citar:

SOUZA, G. ***Study of cirrus clouds physical properties over the state of São Paulo, Brazil, from CALIPSO/CALIOP level 2 data***. 2023. 84 f. Dissertação (Mestrado em Tecnologia Nuclear), Instituto de Pesquisas Energéticas e Nucleares, IPEN-CNEN, São Paulo. Disponível em: ‹http://repositorio.ipen.br/› (data de consulta no formato: dd/mm/aaaa)

Ficha catalográfica elaborada pelo Sistema de geração automática da Biblioteca IPEN, com os dados fornecidos pelo(a) autor(a).

Souza, Giovanni
Study of cirrus clouds physical properties over the state of São Paulo, Brazil, from CALIPSO/CALIOP level 2 data / Giovanni Souza; orientador Eduardo Landulfo. -- São Paulo, 2023.
84 f.

Dissertação (Mestrado) - Programa de Pós-Graduação em Tecnologia Nuclear (Materiais) -- Instituto de Pesquisas Energéticas e Nucleares, São Paulo, 2023.

1. Cirrus Clouds. 2. CALIPSO. 3. CALIOP. 4. Remote Sensing. I. Landulfo, Eduardo , orient. II. Título.

Dedico este trabalho em memória de minha querida Mãe Balbina que sempre me incentivou a estudar.

Acknowledgements

I would like to express my sincere gratitude to Professor Eduardo for his invaluable guidance, support, and friendship throughout my project. I am grateful for his faith in my abilities, for providing countless learning opportunities, and for offering insightful suggestions and discussions to enhance my work. I am also indebted to Dr. Fábio for his patience and mentorship since day one of my master's program. He has been a friend and an excellent teacher, introducing me to the fundamental concepts of lidar and CALIPSO, and always willing to answer my numerous questions.

I am grateful to Professor Boris Barja for his helpful suggestions and discussions on my work and for hosting me during my visit to the University of Magallanes in Punta Arenas. I would also like to thank Tomás Beca for his contributions to my project and for being my walking partner in Punta Arenas.

I owe a debt of gratitude to my friends and group mates Alex, Alexandre Cacheffo, Alexandre Yoshida, Antônio, Elaine, Fernanda, Fernando, Izabel, Jonatan, Zé Carlos, José da Matta (Zé), Pérola, Thaís Andrade and Thaís Corrêa, for their support, collaboration, and for the enjoyable moments of laughter and coffee. Also to my colleagues and friends with whom I shared a room, Armando, Noé, Jhonatha, and Vitoria.

To my dear friend Amanda for all these years of friendship and support. Especially during the quarantine period, when it was very important to keep my mind healthy with online games and conversations.

Finally, I would like to thank my family. My father Manoel, my two brothers Sebastião (Tião) and José Nilton (Zenilton), and my two sisters Maria (Bia) and Carolina (Carol) for their encouragement, love, and respect for my work and study, especially during quarantine.

RESUMO

Medições por satélite tem dado uma enorme contribuição para o desenvolvimento do conhecimento científico. Ao fornecer dados sobre componentes atmosféricos em grandes áreas e longos períodos de tempo, esses instrumentos permitiram aos pesquisadores obter uma compreensão muito mais profunda do meio ambiente. Neste estudo, analisamos dados de nível 2 do satélite CALIPSO/CALIOP para investigar as características físicas e ópticas de nuvens cirrus no estado de São Paulo entre os anos de 2007 e 2017. O estudo mostrou que cirrus é o tipo de nuvem mais presente no região, e se formam principalmente em altitudes entre 10 km e 14 km, e possuem espessura média de 1,4 km. Elas se formam em baixas temperaturas, normalmente abaixo de -40℃. A análise das características sazonais mostrou que a frequência de ocorrência de nuvens cirrus aumenta durante o verão, e coincide com a formação de nuvens convectivas. Isto ocorre devido à formação de cirrus a partir de nuvens do tipo "anvil". A análise de profundidade óptica revelou que o tipo mais comum de cirrus é a cirrus opaca (τ > 0,3), com uma frequência de ocorrência geral acima de 45%. Esses resultados fornecem informações valiosas sobre o comportamento das nuvens cirrus na região e demonstram o importante papel que as medições de satélite podem desempenhar no avanço de nossa compreensão da atmosfera.

Palavras-chaves: Nuvens Cirrus, CALIPSO, CALIOP, Sensoriamento Remoto

ABSTRACT

Satellite measurements have made an enormous contribution to the development of scientific knowledge. By providing data on atmospheric components over large areas and long periods of time, these instruments have enabled researchers to gain a much deeper understanding of the environment. In this study, we analyzed level 2 data from the CALIPSO/CALIOP satellite to investigate the physical and optical characteristics of cirrus clouds in the state of São Paulo between 2007 and 2017. The study showed that cirrus is the most present type of cloud in the region, and they mainly form at altitudes between 10 km and 14 km, and average thickness of 1.4 km. They form at low temperatures, typically less than -40℃. The analysis of the seasonal characteristics showed that the frequency of occurrence of cirrus clouds increase during summer, and coincide with the formation of convective clouds due to the formation of cirrus from anvil clouds. The optical depth analysis revealed that the most common type of cirrus is thick ($\tau > 0.3$), with a overall frequency of occurrence above 45%. These results provide valuable insights into the behavior of cirrus clouds in the region and demonstrate the important role that satellite measurements can play in advancing our understanding of the atmosphere.

Keywords: Cirrus Clouds, CALIPSO, CALIOP, Remote Sensing

LIST OF TABLES

LIST OF FIGURES

List of abbreviations and acronyms

CALIPSO	Cloud-Aerosol Lidar and Infrared Pathfinder Satellite Observation
NASA	National Aeronautics and Space Administration
CNES	Centre National d'Études Spatiales
CALIOP	Cloud-Aerosol Lidar with Orthogonal Polarization
COD	Cloud Optical Depth
LIDAR	Light Detection and Ranging
OD	Optical Depth
WMO	World Meteorology Organization
ICN	Ice Condensation Nuclei
Nd: YAG	Neodymium-doped Yttrium Aluminium Garnet
VMF	Vertical Feature Mask
QA	Quality Assurance
LOT	Low Overcast Transparent
LOO	Low Overcast Opaque
SC_t	Transition Stratocumulus
CUB	Low Broken Cumulus
AC_t	Altocumulus Transparent
ASO	Altostratus
CIR	Cirrus

DCO	Deep Convective

List of symbols

λ	Wavelength
I_λ	Monochromatic intensity
κ	Mass extinction cross section
ρ	Density of the material
α	Extinction coefficient
$O(R)$	Overlap function
$P(R)$	Power of the laser beam
K	Performance factor of the lidar system
$G(R)$	Geometry factor of the lidar system
β	Backscatter coefficient
c	Speed of light
η	Overall lidar system efficiency
τ	Optical Depth

SUMÁRIO

1 Introduction

Clouds play a crucial role in the understanding of the atmospheric system of Earth and the processes of climate change (PROTAT et al., 2009). Knowledge about its properties is essential to improve climate prediction models (DELANOË et al., 2007; STEPHENS, 2005). They affect the climate through their effects on the hydrologic cycle of Earth, as well as through their interaction with the incoming solar radiation and outgoing Earth radiation (WINKER et al., 2010) (Figure 1). The effect of this interaction can cause heating or cooling on the Earth depending on physical and optical properties, such as height, temperature, and optical depth (OD) of the clouds present in the atmosphere (STEPHENS et al., 2002; CORTI; PETER, 2009).

Low and medium-height clouds usually present characteristics that result in the reflection of part of the incoming solar radiation, causing a negative effect on the radiation balance, known in the literature as the albedo effect (BOUCHER; LOHMANN, 1995). On the other hand, high clouds interact less with the incoming solar radiation thus having a lower albedo effect. Most of these high-altitude clouds are a specific type of cloud known as cirrus. Cirrus clouds are thin white clouds, made up mostly of ice crystals and their horizontal extension can reach over 1000 km (HEYMSFIELD, 1975). They form in the upper troposphere (typically at altitudes between 6 and 16 km), where the temperature is usually below -30°C (HEYMSFIELD et al., 2017). Those types of clouds are also known for being optically thin and can be separated by their OD as subvisible ($\tau < 0.03$), thin ($0.03 < \tau < 0.3$), and thick ($\tau > 0.3$) (SASSEN; CHO, 1992). Cirrus clouds interact with the outgoing thermal radiation emitted by the surface of Earth, thus contributing to an increase in the greenhouse effect (LIOU, 1986; WINKER et al., 2009). Because of these unusual characteristics, the interest in studying cirrus clouds has grown in recent decades. Scientists around the world have been collecting information about the physical and optical properties of cirrus. Measurements of this type of cloud can be performed in situ, using aircraft

Figure 1 – Diagram that illustrates the global average energy budget of Earth, showing the different components that contribute to the balance of energy on a global scale. The numbers on the diagram indicate the estimated magnitudes, in units of W/m^{-2}.

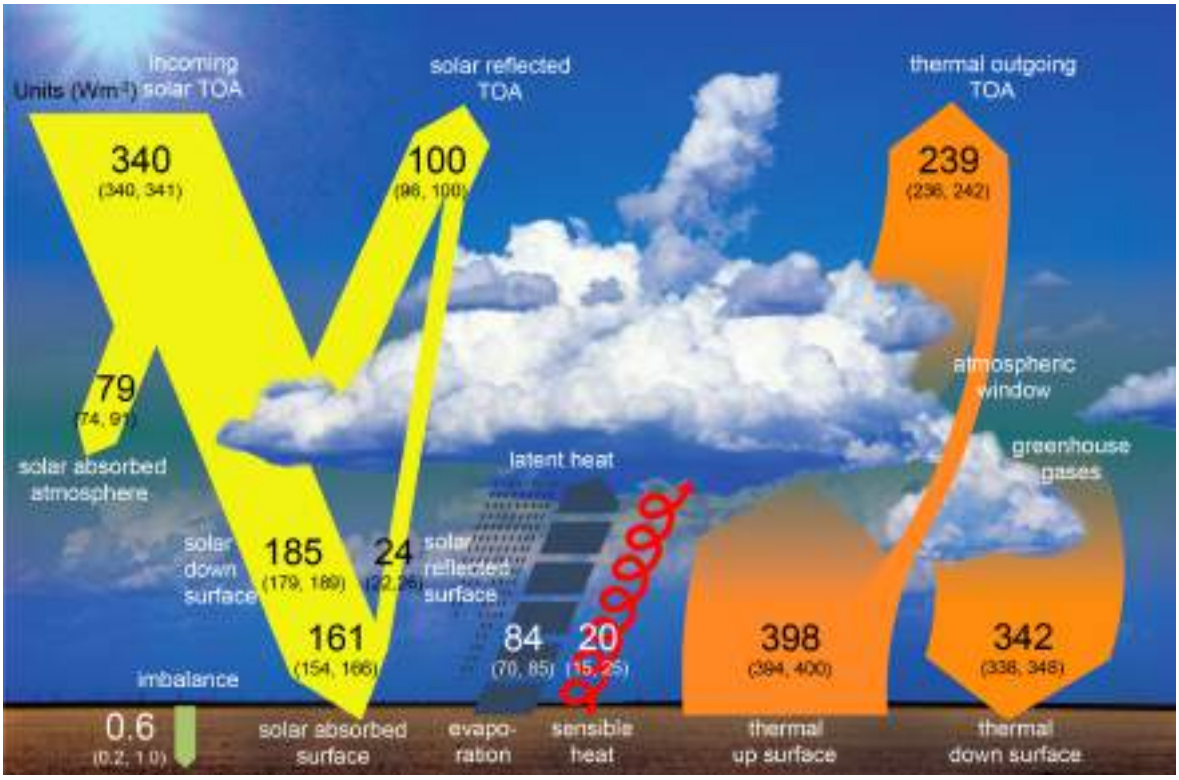

Source: (FORSTER et al., 2021)

or balloons equipped with instruments to map or collect ice crystals (HEYMSFIELD, 1973; ARNOTT et al., 1994; LAWSON et al., 2006; KUHN; HEYMSFIELD, 2016). It is also possible to measure by applying remote sensing techniques, using instruments such as radiometers (OU et al., 1993), cameras operating in the visible spectrum of light (CHEPFER et al., 2002), ground-based lidar systems (GOLDFARB et al., 2001) or, as in the case of this work, using a lidar aboard a satellite.

Satellites have greatly impacted the study of atmospheric components due to their global coverage, enabling the investigation of large-scale phenomena such as clouds. Two commonly used satellites for cloud studies are CloudSat and CALIPSO (Cloud-Aerosol Lidar and Infrared Pathfinder Satellite Observation). CALIPSO is part of a joint mission between NASA and the French space agency CNES (WINKER et al., 2009). Launched in April 2006, CALIPSO orbits the Earth in a polar orbit at an inclination of 98.2°, allowing for global coverage (HUNT et al., 2009). With

a complete scan possible in 16 days and an error smaller than $\pm$10 km, the orbit of the satellite is controllable (WINKER et al., 2009). CALIPSO is equipped with a radiometer and a camera in the visible light spectrum, but the Cloud-Aerosol Lidar with Orthogonal Polarization (CALIOP) is the focus of this work. CALIOP is a lidar that emits laser pulses at wavelengths of 532 nm and 1064 nm and detects the same two wavelengths, with two channels at 532 nm with different polarizations, perpendicular and parallel (VAUGHAN et al., 2009). CALIPSO is part of the A-Train constellation alongside with CloudSat and other satellites focused on atmospheric measurements. CloudSat uses a radar system to observe cloud condensate and precipitation with high resolution (STEPHENS et al., 2002). The measurements from CALIPSO and CloudSat complement each other, and researchers often combine the data to study cloud properties more effectively. The use of satellite data for studying cirrus clouds is favored by the height of cirrus occurrence since lidar and radar have fewer obstacles to cause attenuation before reaching those clouds.

Satellites have been used to study cirrus clouds and have allowed for a better understanding of their properties and variations throughout the atmosphere. One such study by Sassen et al. (2008) used CALIPSO combined with CloudSat to analyze cirrus cloud properties on a global scale. The study analyzed one year of data, from June 2006 to June 2007, to determine the frequency of occurrence, base and top altitude, and temperature of cirrus clouds. The study found that the global average frequency of occurrence for cirrus clouds was 16.7%, with the maximum coverage observed in tropical regions at approximately 60% and the minimum coverage observed in polar regions at less than 5%. The study also found that comparing tropical with polar regions, the average frequency of occurrence for cirrus clouds decreases from about 33% to 7%, median cirrus cloud top heights decrease from 15 to 8 km, cloud base height from 12 to 6 km, cloud thickness decreases from 2.8 to 1.4 km, cloud top temperatures increase from about -55°C to -50°C, and cloud top temperatures increase from about -70°C to -60°C.

In tropical regions, the formation of cirrus is highly influenced by convective clouds, which can extend from 1 to 10 km of altitude. At the top of the cloud, where the temperature is below the freezing point, water droplets start to cool, and cirrus clouds are formed, this process is also known as an anvil. The work of Hartmann & Berry (2017) discusses the effect of anvil clouds on the radiation budget in tropical areas

using data from CALIPSO and CloudSat. The results indicate that while thick tropical clouds have a cooling effect on the energy balance, this effect is counteracted by the warming effect of thin upper-level clouds. The authors suggest that the influence of radiative transfer on the anvil clouds may contribute to the abundance of thin high clouds, which have a positive impact on the radiation budget at the top of the atmosphere.

Studies involving cirrus clouds have also been performed on a regional scale, in tropical regions, such as the work by Rosas & Barja (2014) where they analyzed level 2 CALIPSO data over the Camaguey province in Cuba. They made statistics of the seasonal distribution of cirrus clouds from November 2007 until February 2013 and found that the frequency of occurrence during the rainy season was approximately 40%, compared to 15% during the dry season, and the most frequent occurrence height was between 11 and 14 km. Gouveia et al. (2017) is another study in a tropical region where they studied the properties of cirrus clouds above the Amazon rainforest using one-year data from a ground-based lidar from July 2011 to June 2012. They found that the frequency of occurrence observed was 88% during the wet season and around 50% during the dry season. The diurnal cycle of precipitation is reflected in the daily pattern of cirrus clouds, with a minimum around noon and a maximum in the late afternoon. The mean values for cirrus cloud top and base heights, thickness, and optical depth were (14.3 $\pm$ 1.9) km, (14.3 $\pm$ 1.9) km, (12.9 $\pm$ 2.2) km, (1.4 $\pm$ 1.1) km, and (0.25 $\pm$ 0.46), respectively. The temperature of the region where those clouds were observed was at temperatures as low as -90°C. In the tropical tropopause layer (TTL), cirrus clouds were frequently observed, likely associated with slow mesoscale uplifting or remnants of overshooting convection. The authors also calculated the COD of the cirrus observed, 41.6% were classified as subvisible (τ < 0.03), 37.8% were thin (0.03 < τ < 0.3), and 20.5% were thick (τ > 0.3). This means that in central Amazonia, not only do cirrus clouds occur frequently, but there is also a significant proportion of subvisible cirrus clouds.

One of the most relevant studies of cirrus clouds inside the state of São Paulo is the work from Cordoba-Jabonero et al. (2017). They analyzed coincident measurements between CALIPSO level 2 data and measured data from Lidar systems installed at three different locations from three stations: São Paulo City (MSP, Brazil), Tenerife (SCO, Canary Islands, Spain), and Belgrano II base (BEL, Argen-

tina) to examine the backscattering ratio profiles, top and base heights, COD, and temperatures at the top and base boundaries of the cirrus clouds. The study also showed that the height, thickness, and temperature of subtropical cirrus are greater than those measured in the polar region site. The daily mean COD values for the three stations were in good agreement with literature values, but the variability of the cirrus optical features along the day presents large discrepancies. In comparison with CALIOP data, cirrus clouds were observed at similar altitudes, but differences are found mostly in COD values for subtropical cirrus.

In the current context of global warming and climate change, knowing more about the components of the atmosphere that contribute to the increase of global temperature is important to improve climate prediction models, and thus guide future decisions regarding the control of mean global temperature increase. Despite the importance of cirrus clouds, there are regions on the planet where the physical and optical characteristics of this type of cloud are still uncertain. The southern hemisphere is one of those regions that have little information regarding the behavior of cirrus clouds. Within this problem, the purpose of this work is to analyze eleven years of data (2007-2017) from CALIOP to obtain characteristics such as altitude, thickness, temperature, and COD of cirrus clouds present over the state of São Paulo.

This dissertation is divided as follows, Chapter 2 presents the objectives of the work, Chapter 3 presents the bibliography review of basics concepts applied to this work, Chapter 4 describes the methodology created for performing the analysis of CALIPSO data, Chapter 5 presents the results, and Chapter 6 the discussion of those results. Finally, a conclusion is made about the results and suggested topics for future research and the continuity of this work.

2 Objectives

The objective of this work is to conduct a study on the physical and optics of the cirrus clouds, presenting over the state of São Paulo. To achieve the objective will be analyzed level 2 data from the CALIOP lidar, which is on board the CALIPSO satellite (NASA and CNES). The period study will be between 2007 and 2017 to obtain several parameters: altitude of base and top of cirrus clouds, thickness, COD, and temperature.

3 Literature Review

The interaction between radiation and the atmosphere is a key to understanding the use of remote sensing in atmospheric measurements. This section is a summary of the main concepts addressed in this work starting with the basic concepts about clouds with a focus on cirrus clouds. Furthermore, a brief introduction to scattering, remote sensing, lidar technique, and CALIPSO satellite.

3.1 Clouds

Clouds are a collection of water droplets or ice crystals, or even a joint of both, suspend in the atmosphere. When the amount of droplets or crystals inside a cloud is large, it became visible and people can define a cloud by the fraction of the sky that they cover. With modern instrumentation like the use of satellites, clouds can be defined by their optical depth (OD). The OD or COD (Cloud Optical Depth) is an important parameter to study the cloud effect on the energy budget since the COD represents how much radiation is scattered or absorbed by clouds. Their interaction with both the incoming shortwave radiation and the outgoing longwave radiation clouds help to increase or decrease the temperature of the planet. Clouds also act like a vehicle for the atmosphere, because of their transport of moisture, temperature, and gases over a large distance. Clouds also influence the hydrological cycle of Earth by transporting the water from the atmosphere to the surface through precipitation, which is also important to remove the pollutants from the atmosphere and depositing it back to the surface.

Clouds can be categorized into three categories: cumulus, stratus, and cirrus. These categories were introduced around 1800 by Baptiste Lamarck and Luke Howard (HOWARD, 1803; LAMARCK, 1873). The name "cumulus" (Cu) is derived from Latin and means heap or pile, the main characteristic of cumulus clouds is that they are more vertically extended than horizontally, and the boundary of cumulus

clouds is easily distinguished if there is a group of cumulus clouds in the sky it is possible to see each cloud individually. The vertical extension of the cumulus is due to rinsing air mass also known as convection. In opposition to cumulus, stratus is a type of cloud that is more horizontal than vertical which explain why they are called "stratus" (St) which means flat in Latin. The horizontal extent of stratus clouds is due to large-scale vertical wind motion (ROGERS; YAU, 1989). Therefore, stratus clouds cover a larger portion of the sky, being difficult to distinguish one cloud from the other when looking from the surface. The last category of cloud is cirrus, which in Latin means hair or curl in reference to the hair-like appearance of cirrus. In comparison with the other two types of clouds, cirrus consists of ice crystals, and their horizontal dimension is much larger than their vertical dimension.

The World Meteorological Organization (WMO) defines that those three basic categories can be distinguished into cloud types or "genera", depending on the shape and composition of the cloud they can also be subdivided into "specie". Furthermore, they can be subdivided into "varieties" subject to the degree of transparency and characteristics of their macroscopic elements. In total, there are ten cloud types defined by the WMO (Figure 2) as a mix of all three categories of clouds. Clouds can also be divided into subgroups concerning their altitude. The subgroups where they are usually separated are low-altitude (0-2 km), medium-altitude (2-7 km), and high-altitude (7-11 km). There are also clouds with giant vertical extensions, like nimbostratus (Ns) and cumulonimbus (Cb) shown in Figure 2. The word "Nimbus" in Latin means cloud, but in this context refers to precipitating clouds (LOHMANN et al., 2016). This work considered those ten types of clouds from WMO without subdivisions of "specie" and "varieties" (LOHMANN et al., 2016).

3.1.1 Low-Altitude Clouds

Clouds that form at altitudes below 2 km are known as low-altitude clouds, and they come in several types. Those clouds are formed by water droplets. Stratus and cumulus are found at this height alongside fog and another type of cloud called stratocumulus (StCu). As the name suggests, stratocumulus is halfway between stratus and cumulus clouds, they have flat cloud tops like stratus but their horizontal extension is irregular like cumulus being possible to be distinguished individually.

Fog can be understood as a cloud that touches the ground, and the

Figure 2 – Representation of the ten main cloud types according to the WMO separated by their subgroups of height levels.

Source: (LOHMANN et al., 2016)

most common process of formation is through the radiative cooling of Earth. This happens often in the early mornings of autumn and winter, because of the emission of longwave radiation by the surface which causes the air to cool and start to form condensation when there is sufficient ambient moisture. The vertical extension of fog is usually a few hundred meters and that is why they quickly disappear after the heating caused by solar radiation. Fog also can occur by two other mechanisms, the first is when two air masses with different temperatures and high moist mix together, which is called mixing fog. The second is the advection fog, which happens when moist air passes over a cooler surface.

Understanding the different types of clouds that form at low altitudes is important for predicting weather patterns and studying the Earth's atmosphere (LOHMANN et al., 2016).

3.1.2 Mid-Altitude Clouds

Mid-altitude clouds form between 2 and 6 km and their existence is mostly explained by the slow updraft velocity of air masses. The two main types of cloud present at this altitude are altocumulus (Ac) and altostratus (As), the prefix "alto" means high so these two types are similar to cumulus and stratus but at higher altitudes. Altostratus is uniformly distributed in the sky like normal stratus clouds, one difference is that they have lower OD compared with stratus, but still have higher OD than cirrus. Because of this, the altostratus clouds appear more white and when the sun is behind them it appears diffuse and without clear borders.

Altocumulus exists as separated cloud elements or even rolls in layers and patches. Their formation is also associated with local instability and convection, and their OD is also smaller than stratus clouds (LOHMANN et al., 2016).

3.1.3 High-Altitude Clouds

High-Altitude clouds are constituted by three types of clouds: cirrus, cirrostratus, and cirrocumulus. All three types of high clouds are white and optically thin because of the high concentration of ice crystals inside them. In this type of cloud the ice crystal formation is favored by the low presence of water vapor in higher altitudes (LOHMANN et al., 2016). From now on in this work, what is called "cirrus" includes all three categories of high-altitude clouds to be consistent with other works and the CALIPSO team classification of cirrus (more details in section 4).

3.2 Cirrus Clouds

Cirrus clouds occupy about 16.7% of the entire atmosphere and have a more predominant presence in tropical regions where the occurrence can be above 50% (SASSEN et al., 2008). They play an important role in the planet’s radiation balance due to their interaction with thermal radiation (LIOU, 1986). One of the main characteristics of cirrus is the height at which they form, this type of cloud usually forms at high altitudes (typically above 6 km), cirrus clouds are also optically thin, that is, they have a low COD (typically around 0.03 for visible light spectrum) (LYNCH et al., 2002; SASSEN; CHO, 1992).

Figure 3 – Example of a cirrus cloud.

Source: https://scied.ucar.edu/image/cirrus-clouds.

The three categories discussed before are a good way to start understanding what cirrus clouds are, however, they are purely based on what cirrus clouds look like when seen during the day. Properties such as altitude, temperature, and COD are not part of the definition despite being important characteristics of this type of cloud. Over time, studies on cirrus revealed that a fundamental characteristic for classifying them is their composition. Unlike clouds at low and medium altitudes, which are mostly made up of liquid water droplets, cirrus clouds are made up almost entirely of ice crystals. This is the main feature that makes cirrus clouds different from other types of clouds (LYNCH et al., 2002).

3.2.1 Cirrus Clouds Formation Process

Since cirrus clouds are found at altitudes where the ambient temperature is less than 0° C, the water inside the cloud starts to solidify and so ice crystals can

start to form. This process of formation of ice crystals can occur in some specific ways, focus will be given to the two main processes, namely the homogeneous freezing process and heterogeneous ice nucleation (LOHMANN et al., 2016).

Homogeneous nucleation occurs when there is a spontaneous transition from water vapor to ice within the cloud. This transition can occur in the presence of a condensation nucleus (e.g. a cloud droplet), or a solution droplet (liquid aerosol composed of sulfuric acid or sodium chloride). Or it occurs directly due to thermodynamic conditions of the environment, without requiring the presence of these condensation nuclei. (LOHMANN et al., 2016)

For heterogeneous nucleation to occur, the presence of ice condensation nuclei (ICN) is required. ICN is an aerosol particle that provides a suitable surface for water molecules to be able to bond. The accumulation of molecules associated with the low temperature of the environment causes the production of ice inside the cloud. Heterogeneous nucleation is less common due to the low presence of ICN in the atmosphere since an ICN needs specific conditions for its surface to adhere to water molecules. Because of this, the most common process to occur in cirrus formation is homogeneous nucleation (LOHMANN et al., 2016; CZICZO et al., 2013; LYNCH et al., 2002).

The accumulation of ice crystals transforms into a larger crystal (of the order of 10 μ m) and the accumulation of these larger crystals gives rise to cirrus clouds. The size and shape of the ice crystal also depend on the ambient temperature. The most common shape of ice crystals is the flat type, the accumulation of flat-type crystals forms a larger crystal in the shape of a cylinder. Nearly spherical crystals can also form, although they are the least common. The relationship with temperature is that generally the lower the temperature the larger the ice crystals are as shown in Figure 4 (HEYMSFIELD, 1973; LYNCH et al., 2002; LOHMANN et al., 2016).

Cirrus can also form after the occurrence of a type of cloud known as "Anvil". An anvil is a type of cloud that forms at the top of a cumulonimbus cloud, characterized by a wispy, layered appearance. It gets its name from its shape and consists mainly of ice debris that spreads outward from the convective areas of storms. Anvils do not include the dense, white portions of thunderstorms or the active convective column. They can spread out to create large, widespread cloud layers. Tropical cirrus clouds are believed to originate primarily from cumulonimbus

Figure 4 – Example of ice crystals observed inside a cirrus cloud. In panels A, B, and C the temperature is -20 ° C, in panels D and E the temperature is -40 ° C. Finally, in panel F we have an example of an ice crystal collected in an ice fog also at -40 ° C.

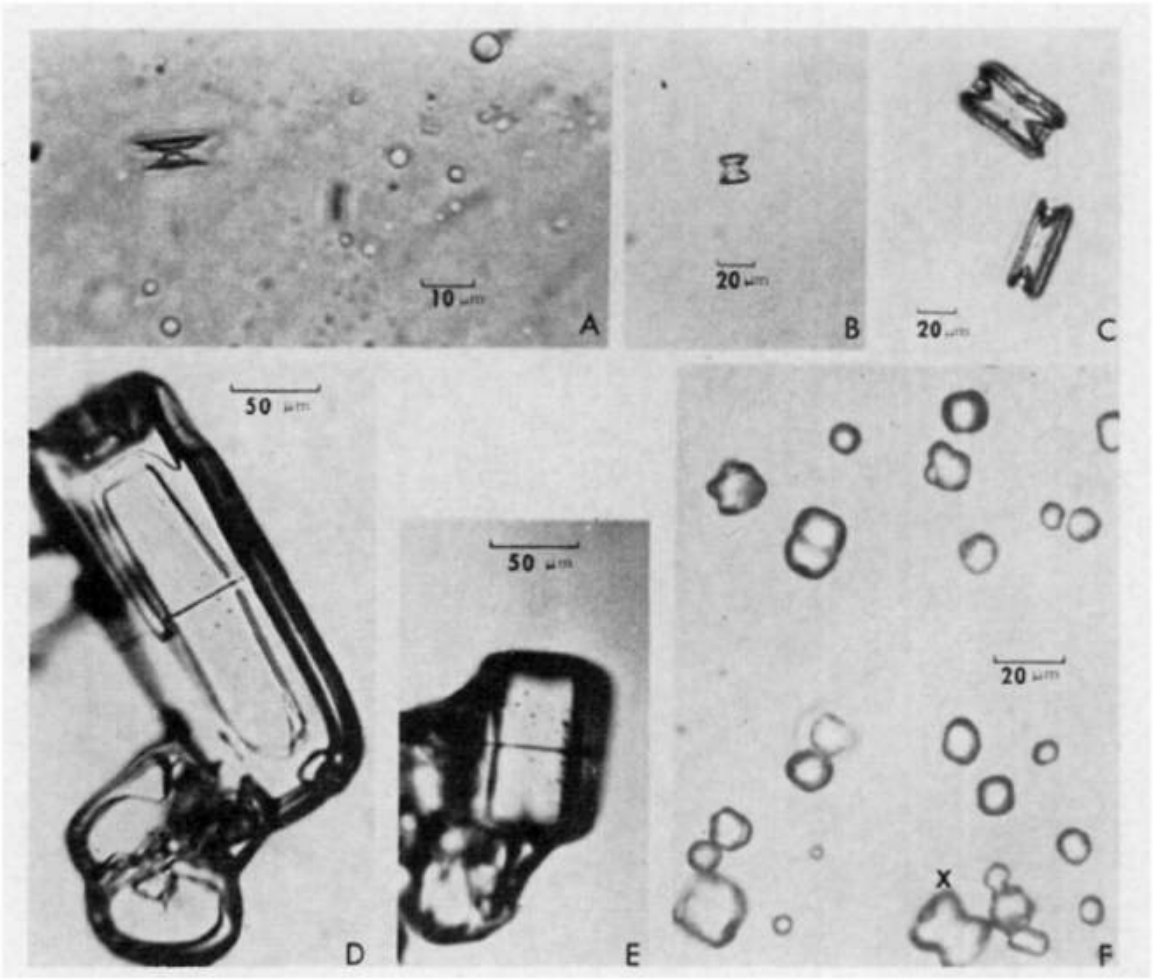

Source: Laboratory and field observations of the growth of columnar and plate crystals from frozen droplets, Heymsfield, A. J. Journal of Atmospheric Sciences, 1973.

clouds. Unlike the thin, wispy cirrus clouds found in mid-latitudes, tropical cirrus clouds have high altitudes and extensive lateral and vertical development, which can have significant radiative effects on the atmosphere and the Earth's surface on a large scale. (LYNCH et al., 2002)

3.3 Radiation Extinction and Scattering

Human beings and other animals are able to see the world because of the capacity of the eye to collect light from the environment. But it is interesting to note

Figure 5 – Example of a thunderstorm reaching a point where it can no longer continue to rise and spreads out horizontally forming an anvil cloud.

Source: <https://www.nasa.gov/topics/earth/features/astronauts_eyes/iss016e27426.html>

that the majority of light collected by the eye is not emitted directly by the light source. We actually see the interaction between the light and the object. This interaction can result in absorption and scattering of the radiation. This is part of the understanding of why we see colors like the blue sky or green grass.

When a beam of light of a certain wavelength λ_0 interacts with a particle there are some different outcomes from this interaction. The light may be reflected, diffracted, or refracted keeping the same wavelength λ_0 (Figure 6). The interaction also can change the income wavelength due to Raman, fluorescence, and thermal emission. For the scope of this work, we consider only the interaction that did not change the wavelength of the emitted radiation, commonly known as the elastic scatter (LIOU, 2002).

Figure 6 – Representation of the possibles outcomes after a radiation of wavelength λ_0 interact with a particle.

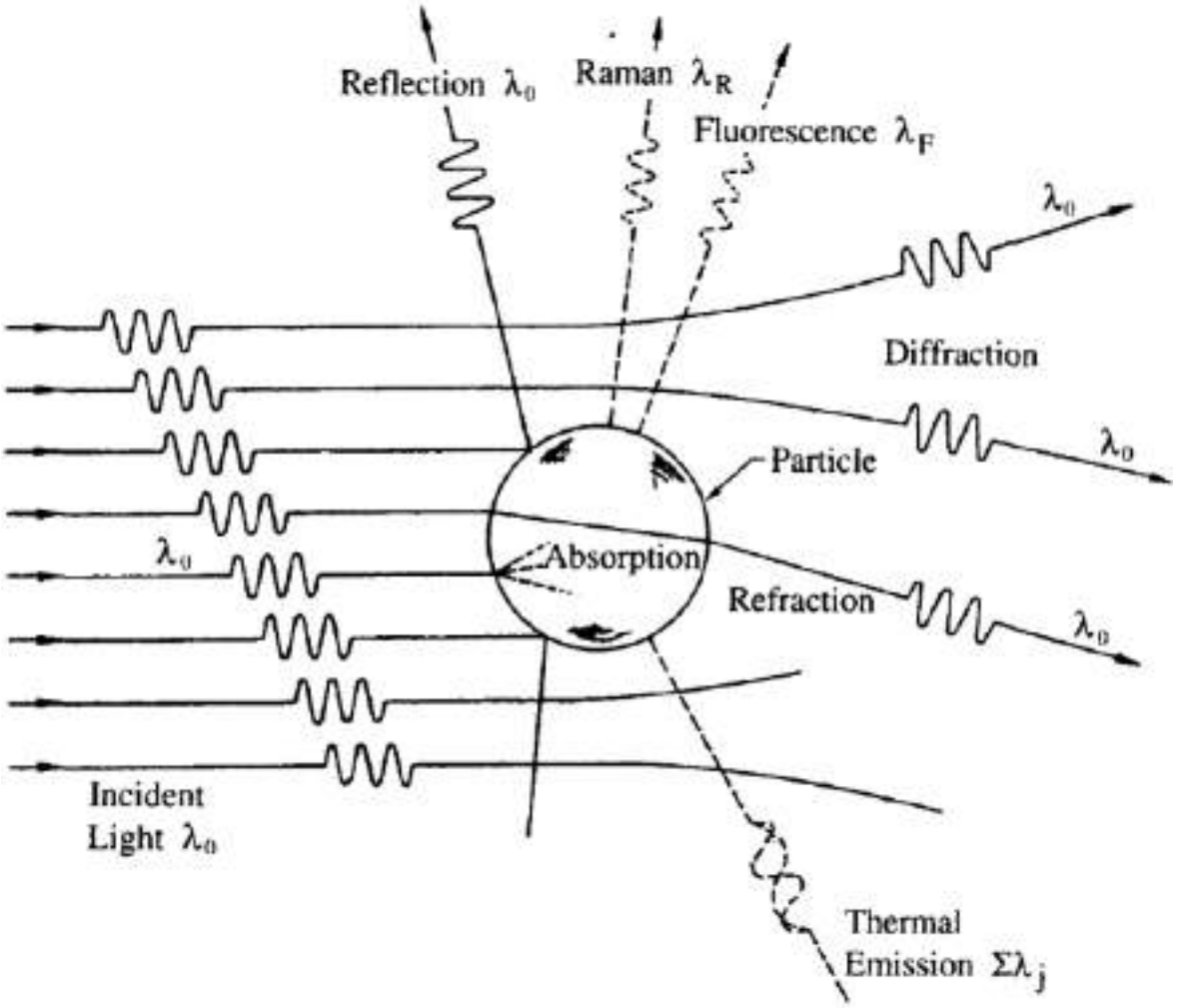

Source: (SEINFELD; PANDIS, 2016)

3.3.1 Transmission and extinction of light inside a material

The interaction between the radiation with some objects depends on the cross-section of the object as well as the intensity of the beam emitted. Suppose we have a beam of intensity $I_\lambda(0)$ that is passing through path S_1 inside a gas chamber. When the beam crosses the chamber it interacts with the gas molecules and there are some outcomes. The beam can pass through the gas, or the beam is absorbed by the gas, or the beam is scattered. At the end of the gas chamber, the intensity of the beam will attenuate to an intensity $I_\lambda(S_1)$:

If we divide the chamber into small parts of size ds we say that the intensity of the beam after passing ds is going to be $I_\lambda + dI_\lambda$ which can be written as:

Figure 7 – Simplified diagram of a light beam passing through a chamber of length S_1.

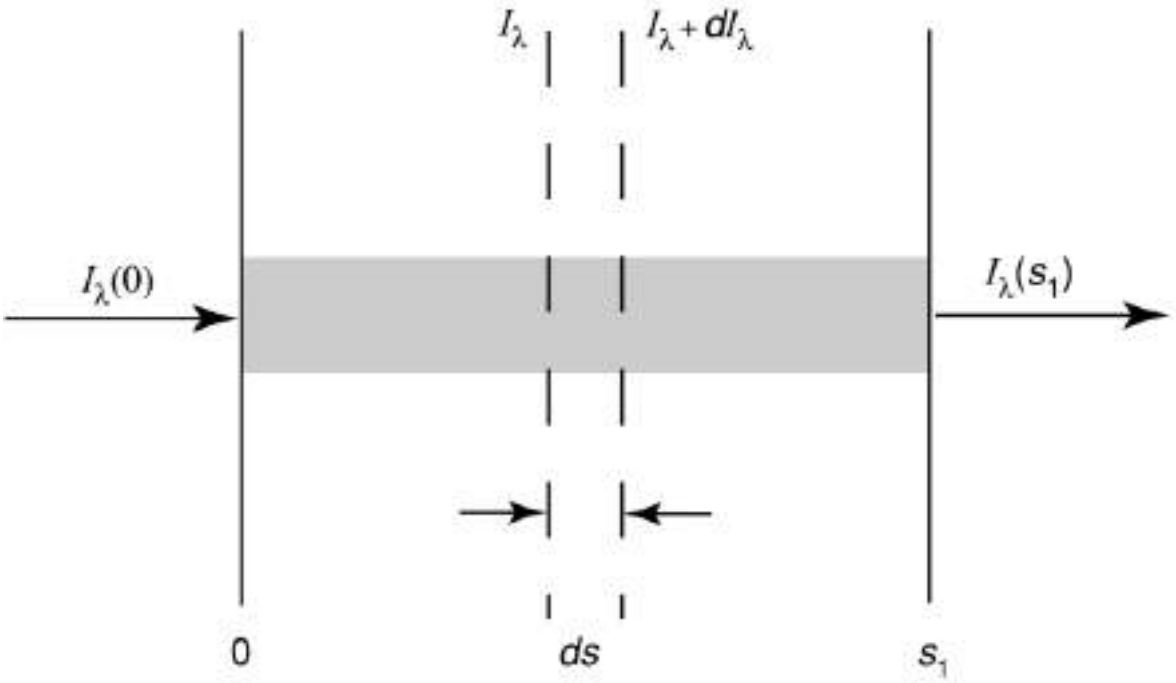

Source: (LIOU, 2002)

$$dI(\lambda, s) = -\kappa(\lambda)\rho I(\lambda, s)ds \tag{3.1}$$

where $\kappa(\lambda)$ is the mass extinction cross section, and ρ is the density of the material. We can write equation 3.1 as:

$$I(\lambda, s) = I_0(\lambda)exp\left(-\int_0^{S_1} \kappa(\lambda)\rho ds\right) \tag{3.2}$$

The equation 3.2 describes how the intensity of the beam decreases by an exponential function, this expression is called Beer-Bouguer-Lambert law. From equation 3.2 we can derive two important variables, the transmittance (T) which states how well the environment can transmit radiation:

$$T = \frac{I(\lambda, s)}{I_0(\lambda)} \tag{3.3}$$

The second is the OD usually represented by the Greek letter τ :

$$\tau(\lambda) = -\int_s^{s_1} \kappa(\lambda)\rho ds = -\int_s^{s_1} \alpha(\lambda) ds \tag{3.4}$$

where $\alpha(\lambda)$ is the extinction coefficient, which is a variable that represents how much the beam is attenuated by the environment (SEINFELD; PANDIS, 2016)

3.3.2 Rayleigh and Mie Scattering

Scattering is the process where a particle that was hit by light subtracts energy from the income light and redirects the energy in another direction. In the atmosphere, there are a lot of particles of different sizes that interact with electromagnetic waves. Those particles can be gas molecules ($10^{-4}\,\mu$ m), aerosols (1 μ m), water droplets (10 μ m), ice crystals (100 μ m), and raindrops or hail (1 cm). The correlation between the size of the particle with the scattering is given by the size parameter (LIOU, 2002):

$$x = \frac{2\pi a}{\lambda} \tag{3.5}$$

where "a" is the radius of the particle. The direction of the scattering also depends strongly on the size of the particles, for smaller particles the scattering occurs equally in all directions as shown in Figure 8(a), for bigger particles the frontal direction starts to be the most probable direction like illustrated in Figure 8(b) and 8(c).

The region that describes the probability of the scattering to occur is called the phase function. The phase function describes the angular distribution of scattered light and is a function of the scattering angle, size, and refractive index of the scattering particle.

When the size parameter is much smaller than one ($x << 1$), the scattering regime is called Rayleigh scattering. In Rayleigh scattering the scattered light undergoes a phase shift and is radiated in all directions with the same frequency as the incident light. The intensity of Rayleigh scattering is inversely proportional to the fourth power of the wavelength of the incident light, which explains why the sky appears blue to our eyes since blue is the shortest wavelength of the visible spectrum of light. Rayleigh scattering also has important implications for remote sensing and

Figure 8 – Representation of scattering phase function for a incident wave of 500 nm interacting with particles in three different sizes: a) $10^{-4}\,\mu$ m, b) 0.1μ m and c) 1μ m.

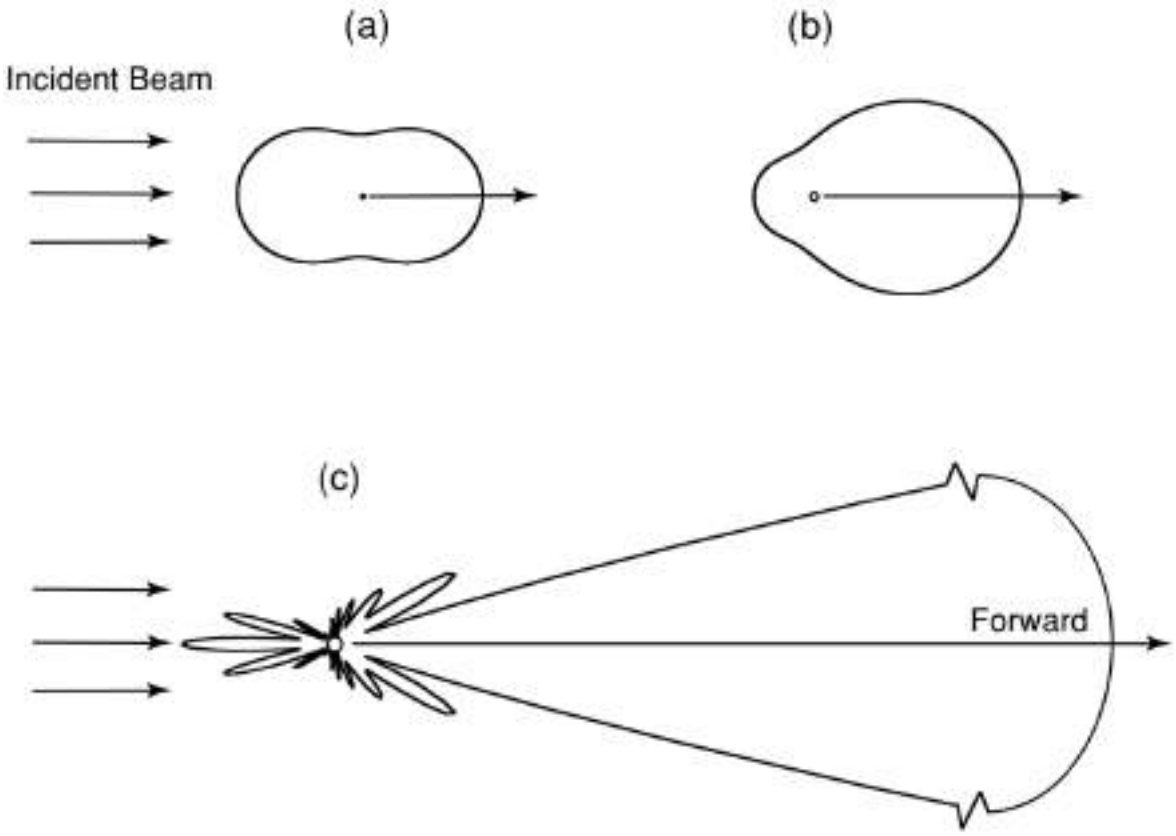

Source: (LIOU, 2002)

atmospheric measurements. Since the amount of Rayleigh scattering is proportional to the amount of air in the atmosphere, it can be used to measure atmospheric density and pressure. It can also be used to correct the attenuation of laser beams used in lidar remote sensing, which allows for more accurate measurements of atmospheric properties.

Mie scattering occurs when the size parameter is comparable with the size of the particle ($x \geq 1$). Examples of such particles in the atmosphere include cloud droplets, raindrops, and aerosols. Mie scattering is characterized by a more complicated scattering phase function than Rayleigh scattering (vide Figure 8(c)). The intensity of light scattered by the Mie process is also wavelength-dependent, but the dependence is much weaker than for Rayleigh scattering. In general, the scattering cross section for Mie scattering is much larger than that for Rayleigh scattering, which means that Mie scattering is more efficient in removing radiation

from the direct beam of sunlight. Mie scattering can be used to derive information about the size and composition of particles in the atmosphere. For example, the presence of cloud droplets can be inferred from the sharp forward scattering peak in the phase function, while the size distribution of aerosols can be determined from the wavelength dependence of the scattering cross section (LIOU, 2002).

3.4 Remote sensing

Remote sensing is a way of retrieving information from an object without physically touching it. This technique is useful when working with an object that is very far or is very hard to collect. Remote sensing techniques take advantage of the capacity of matter to scatter and emit radiation, and the idea is to analyze the radiation emitted from the target. This radiation can be the radiation from a light source, (e.g. the sun) reflected by the object or radiation emitted by the object acting as a blackbody.

There are two types of remote sensing measurement, the first one consists of systems that are designed to only measure a certain range of wavelengths emitted from the object called passive remote sensing. The second one consists of systems that induce the scattering on the object by emitting radiation that interacts with the object and then comes back to the instrument, this is called active remote sensing.

3.4.1 Lidar Technique

Lidar technique is an active remote sensing technique in which its operation is similar to conventional radar and can be understood as laser radar. The technique consists of emitting a laser pulse that will interact with any object that is on its path. As mentioned before the interaction of the radiation with any substance or body can result either in scattering or absorption of the emitted radiation. In case of happening scattering, part of the laser pulse scattered can return in the same direction which was emitted, it is said that the radiation was backscattered by the object. Such property of matter can be used to retrieve information about the object without having to be physically touched. So this is an interesting technique for studying objects that are far from the source of laser emission and also objects that interact strongly with electromagnetic waves. Because of this, the lidar system is very

efficient for studying the components of the atmosphere, such as gas, particles, dust, clouds, and other atmospheric components (WEITKAMP, 2006).

When emitting the laser pulse towards the atmosphere, the components in suspension in the atmosphere can interact with the pulse by scattering, absorbing, or both at the same time. In the experimental setup of the lidar, a telescope is responsible for collecting the backscattered component of the pulse, and then redirecting the signal to a photodetector especially designed to measure the backscattering signal of the emitted pulse and convert the light signal into an electrical signal which is finally interpreted by an acquisition computer (KOVALEV; EICHINGER, 2004; WEITKAMP, 2006). A simplified diagram of a standard lidar assembly is shown in Figure 9.

Figure 9 – Simplified diagram of the experimental setup for a lidar system with the transmission system (laser), receiver system (telescope), and acquisition system (detector).

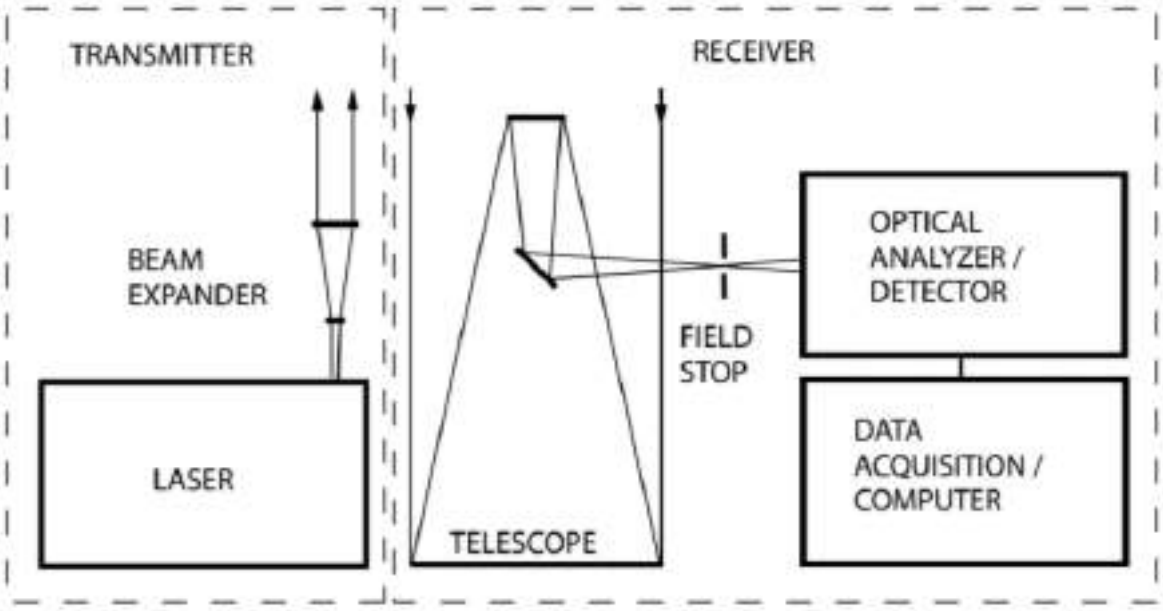

Source: Lidar: range-resolved optical remote sensing of the atmosphere, Weitkamp, C. Springer Science & amp; Business, 2006.

Depending on the type of interaction the light has with the atmospheric component, the wavelength of the backscattered light may be different from the emitted light. This type of scattering is known as Raman scattering (LIOU, 2002). Most studies of the atmosphere are focused on aerosols and clouds, which scatter light in the same wavelength as the emitted light, also known as elastic scattering (WEITKAMP, 2006). The focus of this work will be on the most common type of lidar,

which is the elastic lidar.

The laser wavelength used can vary between 250 nm and 11 μ m depending on the purpose for which it will be used. In the early years of lidar use, it was common to use ruby, nitrogen, copper vapor, and CO_2 in laser production, but nowadays it is common to use a crystal called Nd: YAG (Neodymium-doped Yttrium Aluminium Garnet) because this crystal emits in the infrared spectrum, in the length of 1064 nm. Nonlinear Crystals are used to double, triple, or even quadruple the frequency of the pulse emitted by Nd: YAG and thus obtain the wavelengths of 532, 355, and 266 nm (WEITKAMP, 2006).

The telescope used as the receiver of the backscattered signal has a diameter that can vary from 0.1 m to a few meters, and the diameter of the telescope dictates the efficiency of the system. The distance at which the telescope is positioned from the laser is important and can be placed on the same optical axis. The system where the telescope is placed at a certain distance from the laser source is called bi-axial, and when positioned on the same optical axis as the laser it is called mono-axial (WEITKAMP, 2006).

The range of a lidar system is influenced by various geometric parameters that are specific to each system, such as the position of the telescope relative to the laser and the diameter of the telescope. At short distances, the detector cannot fully capture the laser beam, leading to a loss of some of the signal. The extent of this signal loss is determined by factors such as the shape, diameter, and divergence of the laser beam, as well as the diameter, focal length, and field of view of the telescope. The lowest observable range is determined by the region where the laser emitted by the system partially or fully overlaps with the telescope's field of view. This overlapping region is referred to as the overlap function, which is used in the lidar equation to compensate for the system's imperfect spatial resolution and inability to differentiate between adjacent atmospheric volumes (Figure 10). The overlap function measures the portion of the laser pulse volume that interacts with the atmospheric volume being probed by the lidar. The equation for the overlap function is determined by the transmitter and receiver fields of view, the divergence of the lidar beam, and the distance to the scattering volume. There are several techniques for estimating the overlap function, including using hard targets, Rayleigh scattering, and atmospheric molecules (WEITKAMP, 2006).

Figure 10 – Representation of the overlap function between the transmission system (T) and the receiver system (R). The overlap is only considered full when O(R)=1.

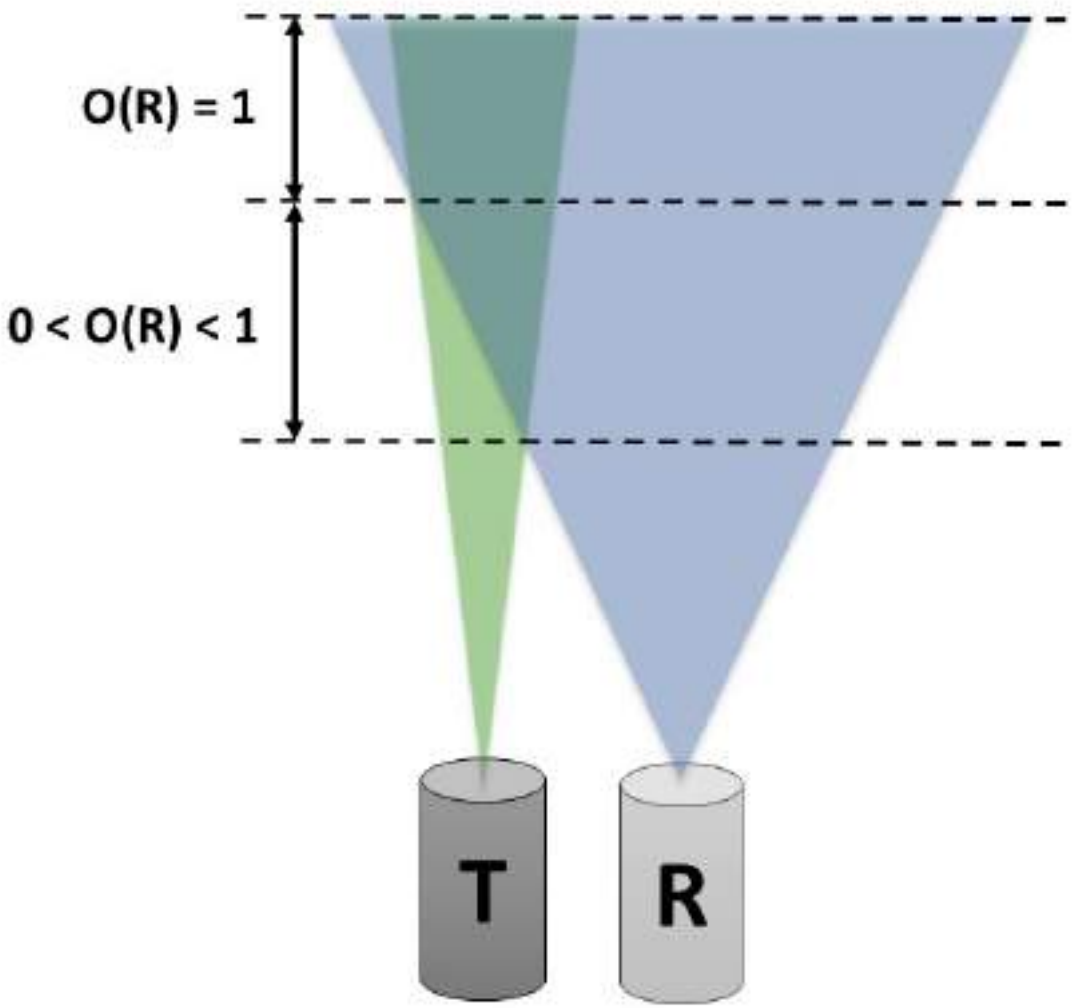

Source: Author

3.4.2 Lidar Equation

To interpret and reconstruct the received signal, the general equation of the lidar is used:

$$P(R) = KG(R)\beta(R)T(R) \tag{3.6}$$

The power P of the laser beam backscatter from a distance R from the

source is dependent on four parameters. Both K and G(R) are parameters determined by the experimental setup of the lidar system, being K the performance factor of the system and G(R) dependent on the geometry of the system. The other two are measurable quantities from the atmosphere, where $\beta(R)$ can be understood as the capacity of the atmosphere components to scatter light in the same direction that was emitted called the backscatter coefficient from a distance R. The term T(R) accounts for the light that is absorbed or scattered in other directions away from the telescope. We can write K as:

$$K = P_0 \frac{ct}{2} A\eta \tag{3.7}$$

where P_0 is the average power per pulse, c is the light speed, t is the temporal pulse length, A is the area of the mirror of the telescope, η is the overall system efficiency and the 1/2 factor is due to the laser beam going to the atmosphere and back to the telescope. The geometric factor G(R) is written in terms of the overlap function O(R) and the loss of energy of the laser beam which is the inverse of distance R squared (R^{-2}):

$$G(R) = \frac{O(R)}{R^2} \tag{3.8}$$

Now we can rewrite equation 3.6 with all parameters in terms of R and λ:

$$P(R,\lambda) = P_0 \frac{ct}{2} A\eta \frac{O(R)}{R^2} \beta(R,\lambda)\, exp\left[-2\int_0^R \alpha(r,\lambda)dr\right] \tag{3.9}$$

In the atmosphere there is the presence of molecules and particles, both contributing to the scattering and absorption of the radiation so the terms of backscatter and extinction must take into account their effect. The term $\beta(R,\lambda)$ represents the backscatter coefficient and can be written as:

$$\beta(R,\lambda) = \beta_{mol}(R,\lambda) + \beta_{aer}(R,\lambda) \tag{3.10}$$

where "mol" is short for molecule and "aer" is short for aerossol. The term $\alpha(r, \lambda)$ is known as the extinction coefficient, and it represents the total radiation that is absorbed and scattered in other directions

$$\alpha(r, \lambda) = \alpha_{mol,sca}(r, \lambda) + \alpha_{mol,abs}(r, \lambda) + \alpha_{aer,sca}(r, \lambda) + \alpha_{aer,abs}(r, \lambda) \quad (3.11)$$

where "abs" is short for absorption and "sca" is short for scattering.

This experimental setup is the basis of any instrument that uses lidar as an acquisition system and can be used fixed to the ground, on board an airplane, or in satellites such as CALIPSO.

3.5 Satellite Based Lidars

The use of ground-based lidar showed to be useful for studying the atmosphere, and the next step was to implement such measurements in aircraft and satellites. There were some satellites in the 60s and 70s using passive instruments and radars for studying the atmosphere. Adding lidars to those measurements was a natural step for spaceborne measurements and the first spaceborne lidar measurements were made in 1994 by the NASA mission LITE (Lidar In-space Technology Experiment) (WEITKAMP, 2006). LITE was a lidar with three wavelengths (355, 532, 1064 nm) designed for atmospheric studies, the main goal of the project was to explore applications of spaceborne lidar (WINKER et al., 1996). Besides LITE, the mission ICESat (Ice, Clouds, and Land Elevation Satellite) launched in 2003 had a lidar instrument on board. The lidar system on board ICESat was GLAS (Geoscience Laser Altimeter System) and it was also used to study the atmosphere using backscatter lidar with the wavelengths of 1064 and 532 nm (ABSHIRE et al., 2005). Those two missions were very important for the development of the lidar technique making way for new missions like CALIPSO.

3.5.1 CALIPSO/CALIOP

The CALIPSO satellite was launched in April 2006 and began operation in June of the same year. Its orbit around the Earth occurs at about 705 km altitude in a polar and sun-synchronized orbit. In one day, CALIPSO travels 14.55 times around the Earth, covering the entire globe in 16 days (WINKER et al., 2007). The satellite is part of the A-Train constellation (Figure 11) which is a set of satellites that are focused on studying the effects of clouds and aerosols on the global climate (STEPHENS et al., 2002; ANDERSON et al., 2005).

Figure 11 – Representation of the A-train constellation and the satellites Aura, CloudSat, CALIPSO, Aqua, GCOM-W1, and OCO-3.

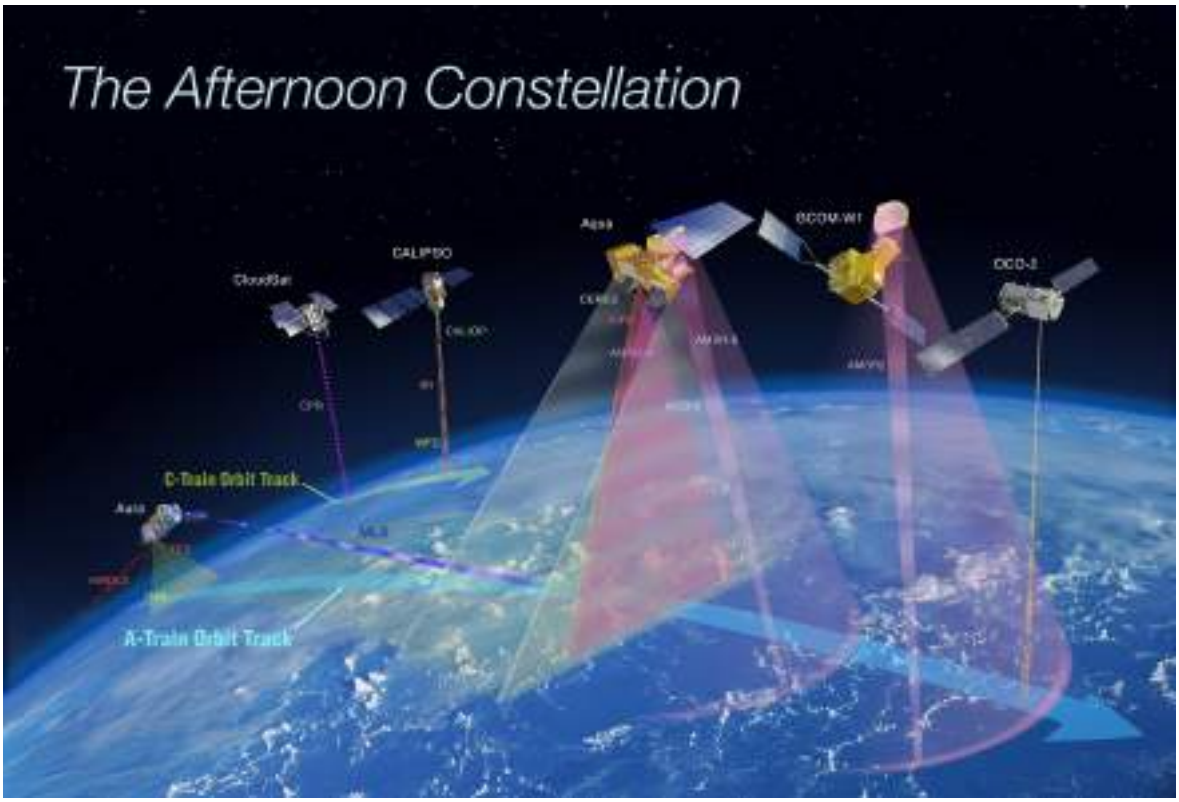

Source: <https://atrain.nasa.gov/>

The main instrument on board the CALIPSO satellite is its lidar called CALIOP (Figure 12) but it also carries two passive instruments, a wide-view camera operating in the visible spectrum of light (at 650 nm) and a spatial resolution of 125 meters/pixel, and an infrared imaging radiometer having three channels with a spatial resolution of 1 km and a sweep of up to 61 km (WINKER et al., 2009).

Figure 12 – On the left is a representation of CALIPSO satellite. On the right side a diagram of the payload with all three instruments.

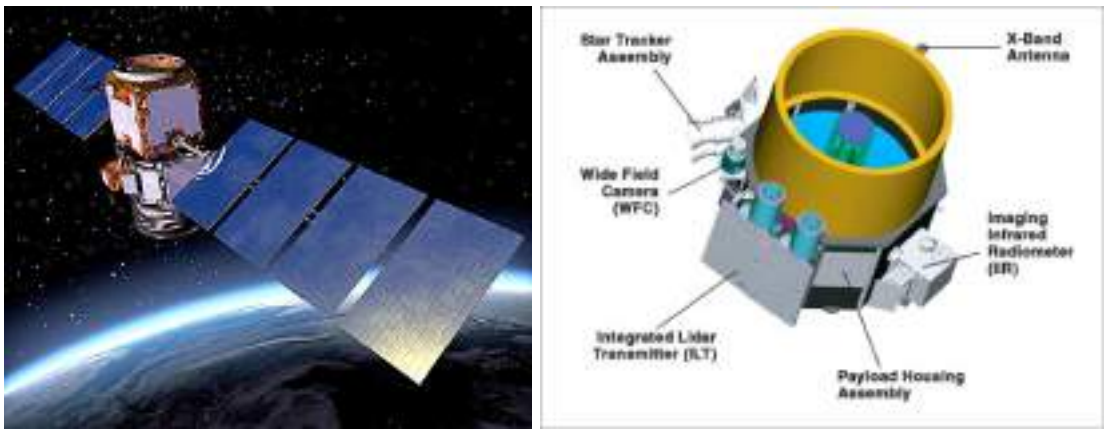

Source: <https://www.eoportal.org/satellite-missions/calipso#sensor-complement>

CALIOP has a diode-pumped Nd: YAG laser operating at a wavelength of 1064 nm, generating the second harmonic signal at 532 nm. Each pulse has a time of emission of 20 ns at a repetition rate of 20.16 Hz. The energy per pulse is 220 mJ for 1064 nm and 110 mJ for 532 nm, measured by sensors placed at the output of each wavelength. The lasers are inside a compartment filled with dry air at standard atmospheric pressure (HUNT et al., 2009). The backscatter signal is collected by a telescope measuring 1 meter in diameter and covering a region on the surface measuring 90 m in diameter. The return signal at 532 nm detected by the telescope passes through a beam splitter that separates it into two separate signals, with opposite polarization. The signal received from 1064 nm goes straight to the sensor, without interference. For the detection of 532 nm signals, both parallel and perpendicular, photomultipliers have a large linear dynamic range, high quantum efficiency, and low dark current. In the infrared channel, an avalanche photodiode is used, which also has a high dynamic range and a good quantum efficiency, however, the dark current is higher in relation to the values of photomultipliers (HUNT et al., 2009; WINKER et al., 2009).

4 Methods

4.1 CALIPSO Products

There are two main types of data produced by the CALIPSO satellite, level 1B and 2, both have some versions that were released throughout the project and which continue to be updated. In this work, the focus is level 2 data but it is important to understand the basics of level 1B.

4.1.1 Level 1B Data

Level 1B data is processed, reconstructed, and geo-located profile data that also undergo corrections and calibrations at full resolution. The data has a horizontal resolution of 333 m and a vertical resolution of 30 m. Level 1B data provides profiles of the total attenuated backscatter profile at 532 nm, which is given by the sum of the channel profiles perpendicular and parallel at 532 nm, the perpendicular attenuated backscatter profile at 532 nm, and the attenuated backscatter profile at 1064 nm (HOSTETLER et al., 2006). Those profiles are corrected due to attenuation when passing through the atmosphere in the following manner:

$$\beta^*(\lambda, z) = \beta(\lambda, z)T^2(\lambda, z) \tag{4.1}$$

where $\beta^*(\lambda, z)$ is the corrected backscatter, T^2 is the two-way transmittance and $\beta(\lambda, z)$ is the same as in equation 3.10. Thus the profile products are defined by the following equations:

$$\beta^*_{532,Total}(z) = [\beta_{532,\parallel}(z) + \beta_{532,\perp}(z)]T^2_{532}(z) \tag{4.2}$$

$$\beta^*_{532,\perp}(z) = \beta_{532,\perp}(z)T^2_{532}(z) \tag{4.3}$$

$$\beta^*_{1064}(z) = \beta_{1064}(z)T^2_{1064}(z) \tag{4.4}$$

In addition, Level 1B data provides profiles of time, longitude, and latitude, as well as information about the satellite's orbit. The use of data from level 1B in this work was to better understand CALIOP and the type of data produced by it. The total attenuated backscatter profile was used to generate atmosphere visualization graphs, also called quicklooks or curtain charts (Figure 13).

Figure 13 – Quicklook example of a calipso passage created using Level 1B data.

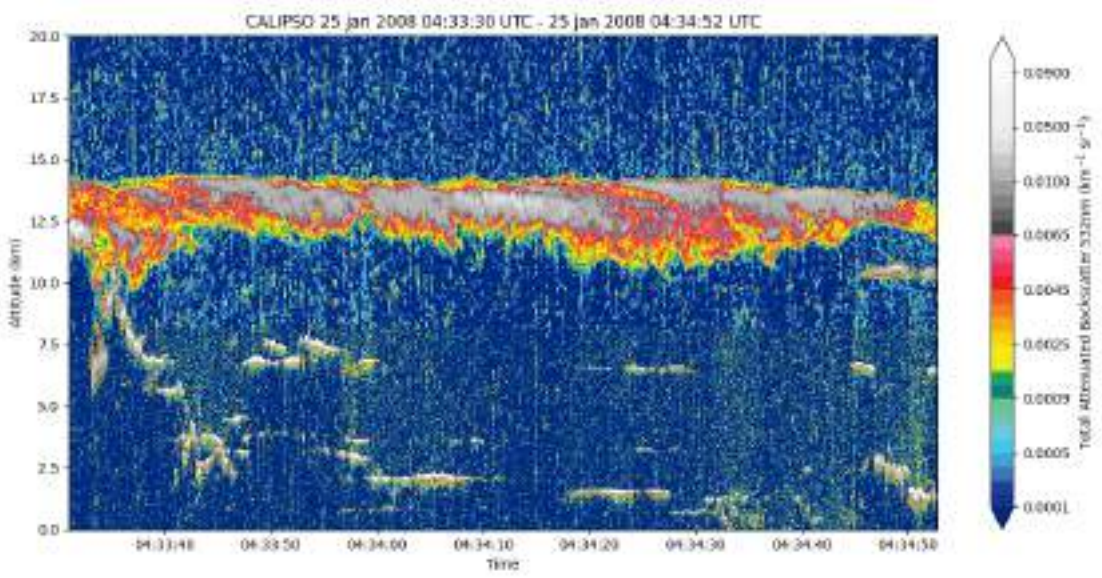

Source: Author

4.1.2 Level 2 Data

Level 2 data is the data that passes for more processing and calculation of physical features. The level 2 fundamental parameters are the altitude of the base and top of cloud and aerosol layers, those information is obtained using the "feature finder" algorithm. In simple terms, the feature finder algorithm determines the atmospheric feature by the analysis of the intensity peaks in the backscatter profiles.

From the lidar profile data, the algorithm also generates basics statistical data called layer descriptors. These descriptors are essential inputs for the scene classification algorithms and for determining the range-resolved optical properties. The detection of backscatter peaks is easier for features that strongly reflect radiation, like stratus and cumulus clouds. But for thin atmospheric components like subvisible cirrus clouds or thin aerosol layers is necessary to average many laser pulses to identify those features. This is done using the algorithm of Selective Iterated Boundary Location (SIBYL), the algorithm conducts several scans of a designated scene, creating attenuated scattering ratio profiles at lower spatial resolutions. After that, the profiles are searched for the presence of clouds or aerosol layers. For more details about CALIPSO algorithms see Vaughan et al. (2005).

4.1.3 Multiple Scattering correction

The majority of lidar retrievals rely on solving the conventional lidar equation (3.9), which employs a single-scatter approximation and disregards the influence of higher-order multiple scattering (KLETT, 1981). Multiple scattering has the potential to cause changes in the apparent extinction or transmittance of the medium. In most lidar systems, the impact of multiple scattering is negligible, allowing these effects to be disregarded without introducing significant errors. However, for satellite lidar systems with their large footprints, multiple scattering effects can be highly significant. Compared to ground-based or airborne lidars with the same field of view, satellite lidars have a footprint diameter of approximately two orders of magnitude larger due to their greater distance from the atmosphere. Consequently, a much larger fraction of the light scattered multiple times contributes to the return signal. As a result, when developing an algorithm to retrieve extinction from satellite lidar data, it is imperative to explicitly consider and account for the influence of multiple scattering effects on the return signal (WINKER, 2003).

In-situ measurements reveal that cirrus clouds consist of ice crystals exhibiting a wide range of shapes and sizes. The specific shapes and sizes are influenced by factors such as temperature, relative humidity, and the dynamics of the cloud layer. Moreover, the sizes and shapes of ice crystals undergo changes throughout their life-cycle processes, including formation, sedimentation, and sublimation. To obtain the multiple scattering factor for CALIPSO data two extreme situations are compared:

a tropical anvil cloud and a polar cirrus. The phase function of the particles inside the cloud for each situation and compared to determine the better approximation for the multiple scattering functions. For more details about the calculation see Winker (2003).

4.1.4 Vertical Feature Mask

The CALIPSO level 2 product has a classification called Vertical Feature Mask (VFM) of the subtypes of clouds and aerosols in a layer. To save space in the files this product is provided in a 16-bit integer where each bit represents a flag that contains information about the data. For example, if we take data where the integer that represents the product is 35842, which in binary forms is:

1000110000000010

now it is necessary to separate the bits to take out the VFM of this profile. To do so, we need to know what each bit represents, and this is described in the table 14.

To separate the bits is used bitwise operation “AND” which is an operation that compares each bit in two binary numbers, if both bits are 1 then the result is 1 but if one of them is 0 then the result is 0. For example, we want to mask the first 3 bits that provide the Feature Type (FT) as shown in table 14, then we need to compare each bit with 1, since we want 3 bits we pick the number 111 (decimal 7):

1000110000000010
0000000000000111
0000000000000010

The result is 10 (decimal 2) which corresponds to a cloud as indicated in table 14. Now that we have the FT we proceed with the bitwise operator “SHIFT RIGHT”, this operator moves bits to the right by the number desired. In this example we want to take out the three bits that we already have:

1000110000000010 –> 1001100000000

repeating this process for the next bits it is possible to obtain all the information of the profile. Following these steps, we have an algorithm to determine the VFM for the whole set of data.

The VFM product provides quality assurance (QA) for each cloud or aerosol classification. The QA is based on the cloud-aerosol discrimination (CAD) score. The CAD score can have a value between -100 and 100, where positive values

Figure 14 – Description of the interpretation of the bits for the VFM product.

Bits	Field Description	Bit Interpretation
1-3	Feature Type	0 = invalid (bad or missing data) 1 = "clear air" 2 = cloud 3 = tropospheric aerosol 4 = stratospheric aerosol 5 = surface 6 = subsurface 7 = no signal (totally attenuated)
4-5	Feature Type QA	0 = none 1 = low 2 = medium 3 = high
6-7	Ice/Water Phase	0 = unknown / not determined 1 = ice 2 = water 3 = oriented ice crystals
8-9	Ice/Water Phase QA	0 = none 1 = low 2 = medium 3 = high
10-12	Feature Sub-type	
	If feature type = tropospheric aerosol, bits 10-12 will specify the aerosol type	0 = not determined 1 = clean marine 2 = dust 3 = polluted continental/smoke 4 = clean continental 5 = polluted dust 6 = elevated smoke 7 = dusty marine
	If feature type = cloud, bits 10-12 will specify the cloud type.	0 = low overcast, transparent 1 = low overcast, opaque 2 = transition stratocumulus 3 = low, broken cumulus 4 = altocumulus (transparent) 5 = altostratus (opaque) 6 = cirrus (transparent) 7 = deep convective (opaque)
	If feature type = stratospheric aerosol, bits 10-12 will specify stratospheric aerosol type.	0 = invalid 1 = PSC aerosol 2 = volcanic ash 3 = sulfate/other 4 = elevated smoke 5 = spare 6 = spare 7 = spare
13	Cloud / Tropospheric Aerosol / Stratospheric Aerosol QA	0 = not confident 1 = confident
14-16	Horizontal averaging required for detection (provides a coarse measure of feature backscatter intensity)	0 = not applicable 1 = 1/3 km 2 = 1 km 3 = 5 km 4 = 20 km 5 = 80 km

Source: <https://www-calipso.larc.nasa.gov/resources/calipso_users_guide/data_summaries/vfm/index_v420.php>

signify clouds and negative values indicate aerosols. The level of confidence in the classification is represented by the magnitude of the CAD score, with a score of

100 indicating complete confidence. Scores with smaller absolute values suggest uncertainty in the classification and a higher chance of error. A score of 0 indicates an equal chance of the feature being a cloud or an aerosol. The QA level of confidence is based on the magnitude of the CAD score (Figure 1). For this work, we have considered only clouds with high QA.

Table 1 – Level of confidence used for the QA based on the magnitude of the CAD score.

Confidence	**Magnitude of CAD score**
high	≥ 70
medium	≥ 50 and < 70
low	≥ 20 and < 50
none	< 20

4.1.5 Cloud Classification

With the VFM it is possible to distinguish clouds with respect to their types and select cirrus. CALIPSO science team separates clouds into types to match the definitions usually found in the literature. They mix some of the types discussed in Chapter 3 based on their opacity and height. Each cloud type is also associated with a numeric category from 0 to 7, which is used to facilitate the storage of the information of the cloud type. In table 2 are shown the types of clouds chosen in VFM and the name based on those ten cloud types discussed before.

Table 2 – Clouds types used in the VFM and the categories of clouds that each cloud type represent.

Abreviation	**Type of cloud**	**Category**
LOT	Low Overcast, Transparent (St, StCu, and fog)	0
LOO	Low Overcast, Opaque (opaque St, StCu, and fog)	1
SC_t	Transition Stratocumulus	2
CUB	Low, Broken Cumulus (trade Cu and shallow Cu)	3
AC_t	Altocumulus (transparent)	4
ASO	Altostratus (Opaque, As, Ns, Ac)	5
CIR	Cirrus (Transparent)	6
DCO	Deep Convective (Opaque As, Cb, Ns)	7

The classification of CALIPSO for transparent clouds is done based on cloud top pressure, height, and cloud fraction (A_c) after the detection of the SYBIL algorithm. Figure 15 summarize the classification algorithm.

Figure 15 – Flowchart to show how the VFM classifies opaque clouds based on the cloud top pressure, height, and A_c.

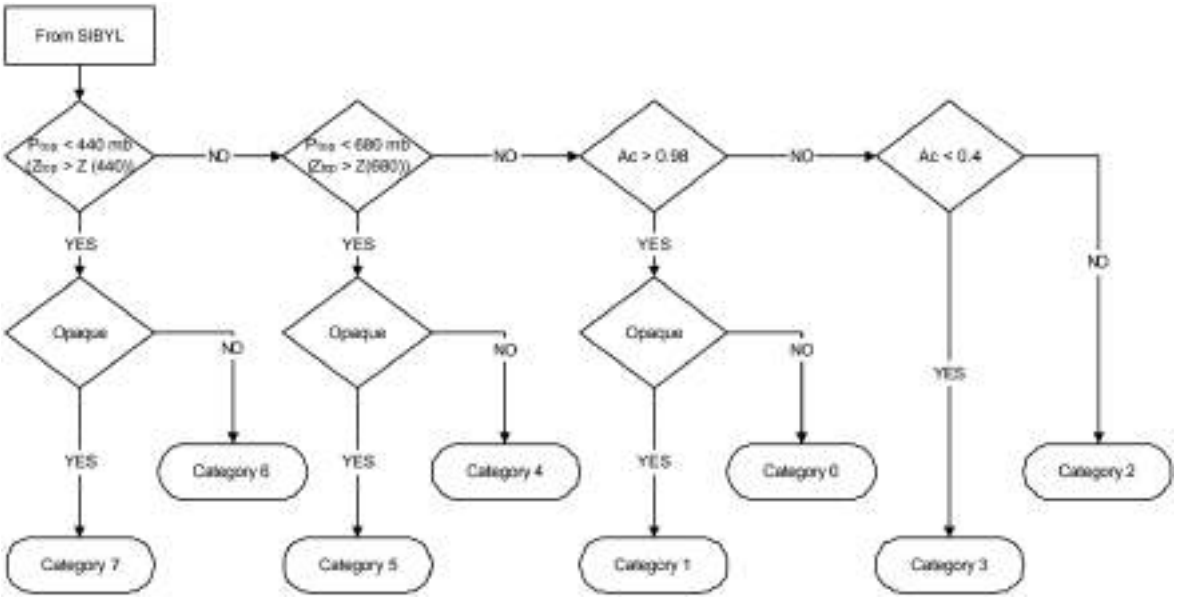

Source: (LIU et al., 2005)

4.2 São Paulo State

The state of São Paulo was selected because of its location. Part of the state is near the Atlantic Ocean, and part is inside the continent (Figure 16), thus having different influences. Besides that, São Paulo is one of the few regions of the country that has other atmospheric instruments, which is interesting for future comparisons.

To select the whole state it was chosen a circular region with a 500 km radius using the application from NASA's website. The circle with the representation of São Paulo State is in Figure 17.

The problem of selecting a circle to select the data is that the boundary of the state is not perfectly circular and a big portion of the states near São Paulo is added to the analysis, as shown in Figure 18.

The latitude and longitude of the satellite were used to ensure that only the passages of CALIPSO inside the state boundary were chosen. To do that, it was calculated if the passage was inside the polygon of the state (Figure 18).

The processes of selection of the data inside São Paulo and the data for analysis are summarized in Figure 20.

Figure 16 – The location of São Paulo state in Brazil.

Source: Author

4.3 South Atlantic Anomaly

The CALIPSO satellite passes over São Paulo about 5 to 6 times a month, which is enough for a whole year to cover almost the entire selected region as shown in Figure 19. According to mission scientists, since 2016 the pressure in the laser compartment has been decreasing and affecting the laser energy (CALIPSO, 2018). This does not affect measurements in various parts of the world, but it is a problem in regions within the South Atlantic Anomaly (SAA) (Figure 22). The SAA is a region where at the same time, the magnetic field of Earth is weaker and there is a region of intense radiation in space near the Earth. This affects mostly spacecraft on a low orbit around the earth (HEIRTZLER, 2002).

Because of this problem, the science team of CALIPSO recommends taking out all profiles with energy shots less than 80 mJ. Since the region of analysis

Figure 17 – The region where the CALIPSO data were selected, corresponds to a 500 km radius circle centered in the state.

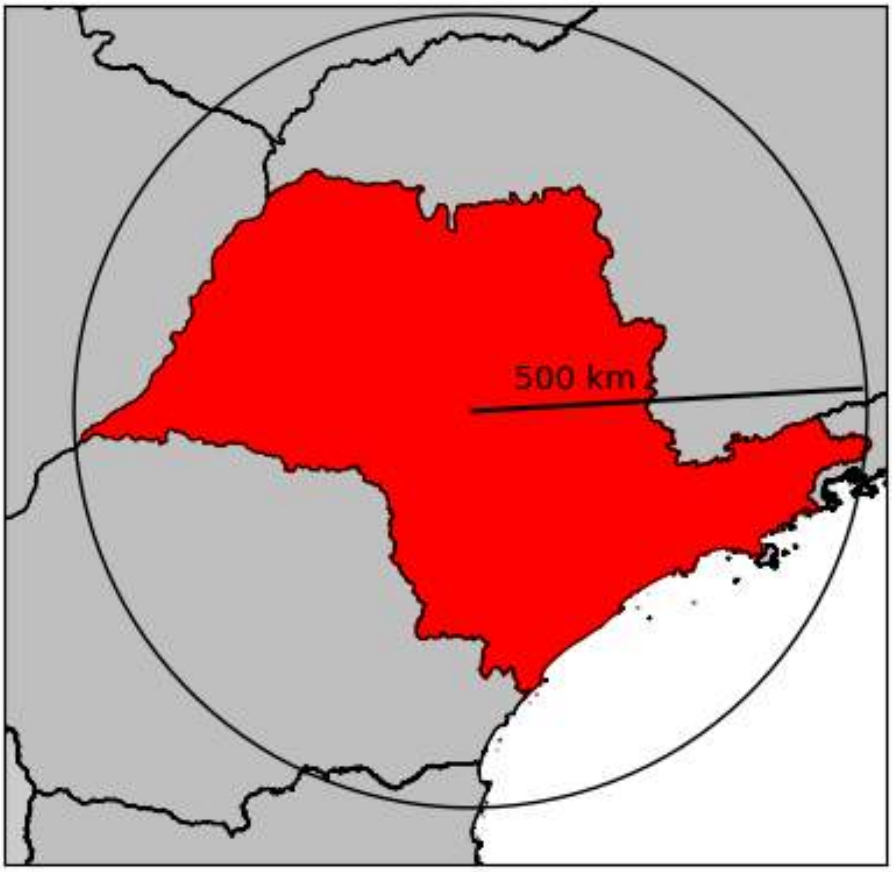

Source: Author

in this work is inside the SAA it will be difficult to analyze CALIOP data in years after 2016, where the effect of SAA is pronounced.

To determine what years are not good to analyze due to the SAA effect over São Paulo, we took the laser energy shots product and selected the profiles with energy shots less than 80 mJ. After that, the percentage of loss for each passage was determined, and the average profile loss per year was calculated.

Figure 18 – One year passage of CALIPSO inside the 500 km radius region centered in the state.

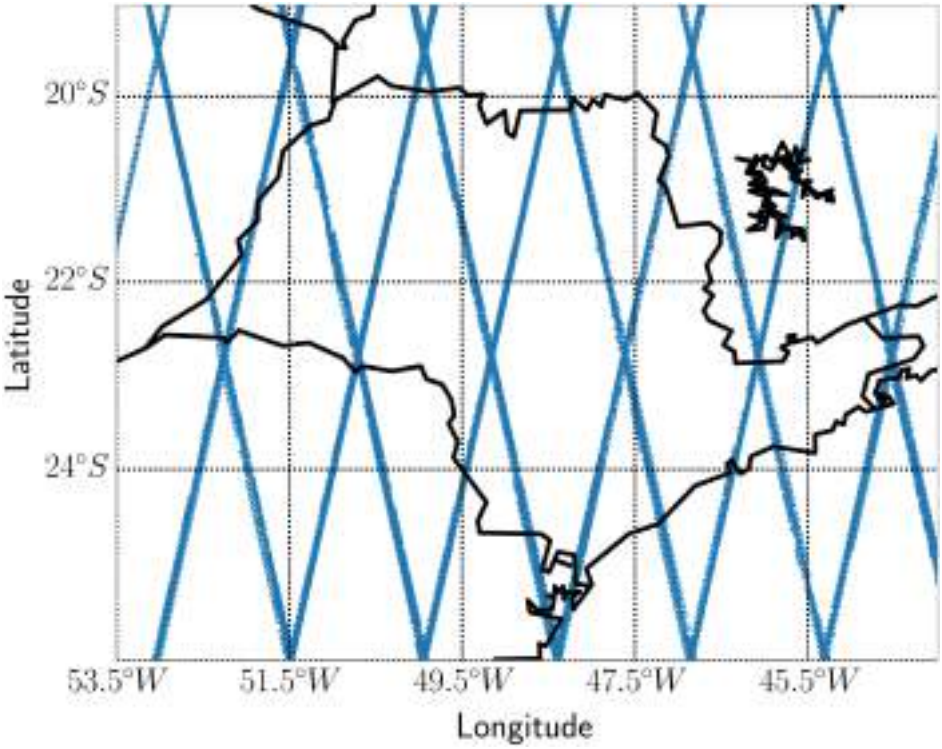

Source: Author

Figure 19 – One year passage of CALIPSO but now only with the passage of the satellite strictly inside the state boundary.

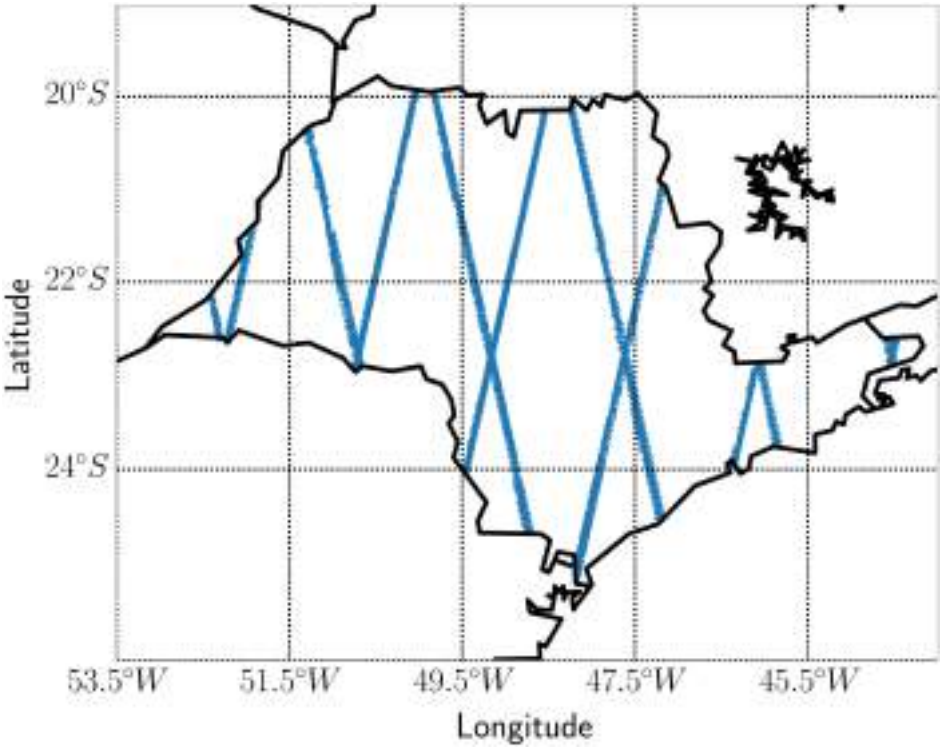

Source: Author

Figure 20 – Flowchart of the analysis scripts.

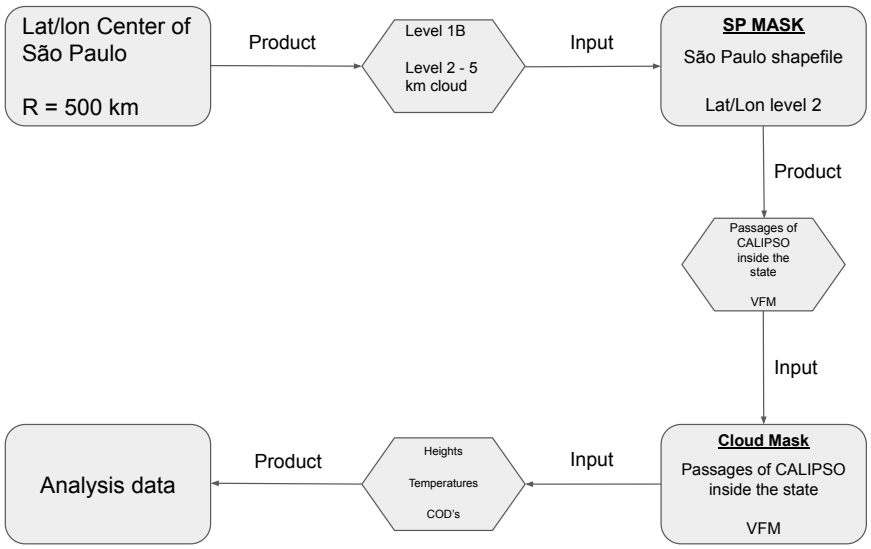

Source: Author

Figure 21 – Representation of the weaker magnetic field over South America compared to the rest of the Earth.

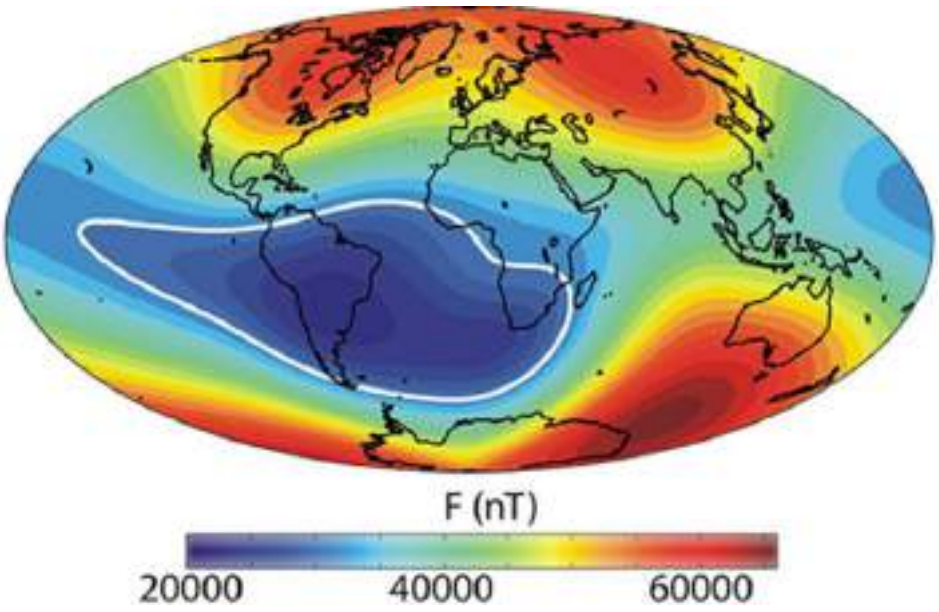

Source: (PAVÓN-CARRASCO; SANTIS, 2016)

Figure 22 – Example of a full CALIPSO passage where the effect of SAA is clear when CALIPSO passes over South America (blue line).

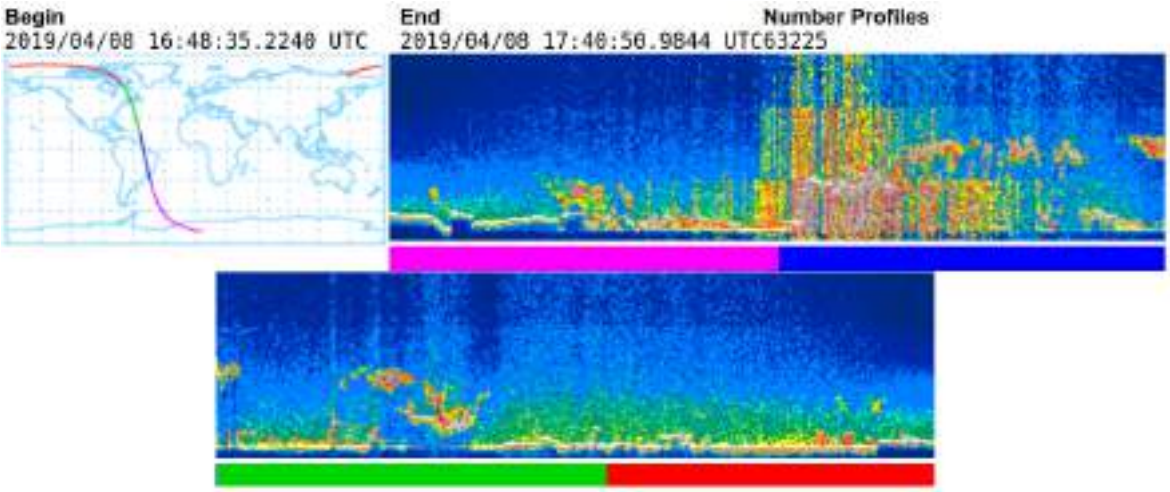

Source: Adapted from <https://www-calipso.larc.nasa.gov/products/lidar/browse_images/std_v4_showdate.php?browse_date=2019-04-08>

5 Results

In this section, we present the physical and optical characteristics of cirrus clouds in São Paulo state based on the analysis of eleven years of data collected by the CALIPSO satellite. Our analysis is divided into two parts: the evolution of these characteristics over the years, and their variation over the months.

5.1 South Atlantic Anomaly Analysis

We used the variable 'Laser Energy 532' from the level 1B data to check if the data was acquired with the proper laser energy. To determine if the profiles were valid, we followed the criterion suggested by the CALIPSO science team, classifying profiles with less than 80 mJ of energy as bad (CALIPSO, 2018). We then calculated the total number of bad profiles for each passage and divided it by the total number of profiles acquired in that passage. This process was repeated for the entire year, and we calculated the average percentage of data lost due to low energy shots in each passage. Figure 23 shows the statistics of the average yearly percentage of data affected by low energy shots when CALIPSO flew over the state of São Paulo.

5.2 Yearly distribution

This section presents the results obtained from analyzing eleven years of CALIPSO satellite data to characterize cirrus clouds in São Paulo state, focusing on their physical and optical properties. The data inside the state was selected, and cloud base was detected using the 'Layer Base Altitude'. Figure 24 shows the total number of cloud layers detected each year, while Figure 25 displays only the cirrus clouds. The VFM classification allowed us to determine the number of clouds detected for each type and year, and their frequency was calculated by dividing the number of clouds detected for each type by the total number of clouds detected in

Figure 23 – Statistics of the occurrence of low-energy shots over São Paulo state throughout the years due to the SAA.

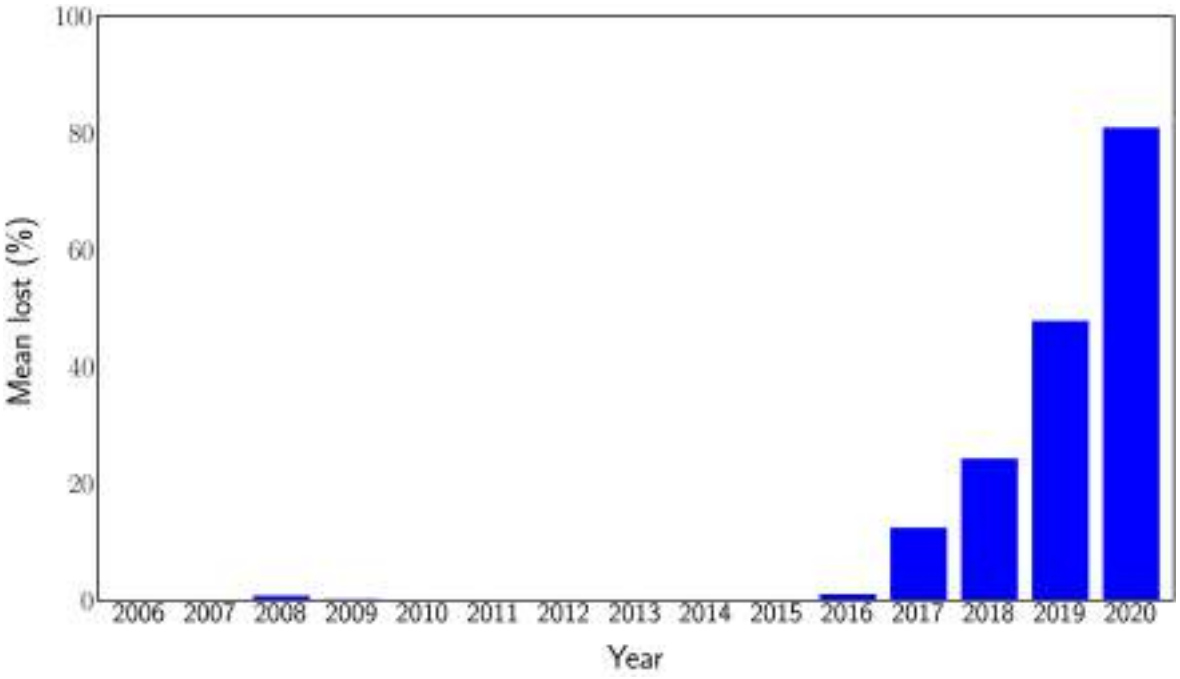

Source: Author

that year, as shown in Figure 26.

The base and top height distribution of cirrus clouds are displayed in Figures 27 and 28, respectively, while the thickness distribution is shown in Figure 29, which is calculated as the difference between the top and base heights. The distribution of cirrus base and top temperatures over the years is illustrated in Figures 30 and 31, respectively. These data are available in the CALIPSO database and were provided by Merra-2.

The frequency of cloud occurrence with respect to altitude was obtained by dividing the number of clouds detected at a certain height by the total number of CALIPSO passages within the state, and the result is presented in Figure 32. The frequency of cirrus occurrence was determined by dividing the number of cirrus clouds detected by the total pass of CALIPSO in São Paulo, as shown in Figure 33. The same approach was used to compare DCO cloud types with cirrus formation, and the result is displayed in Figure 34.

Figure 24 – Total number of cloud layers detect per year.

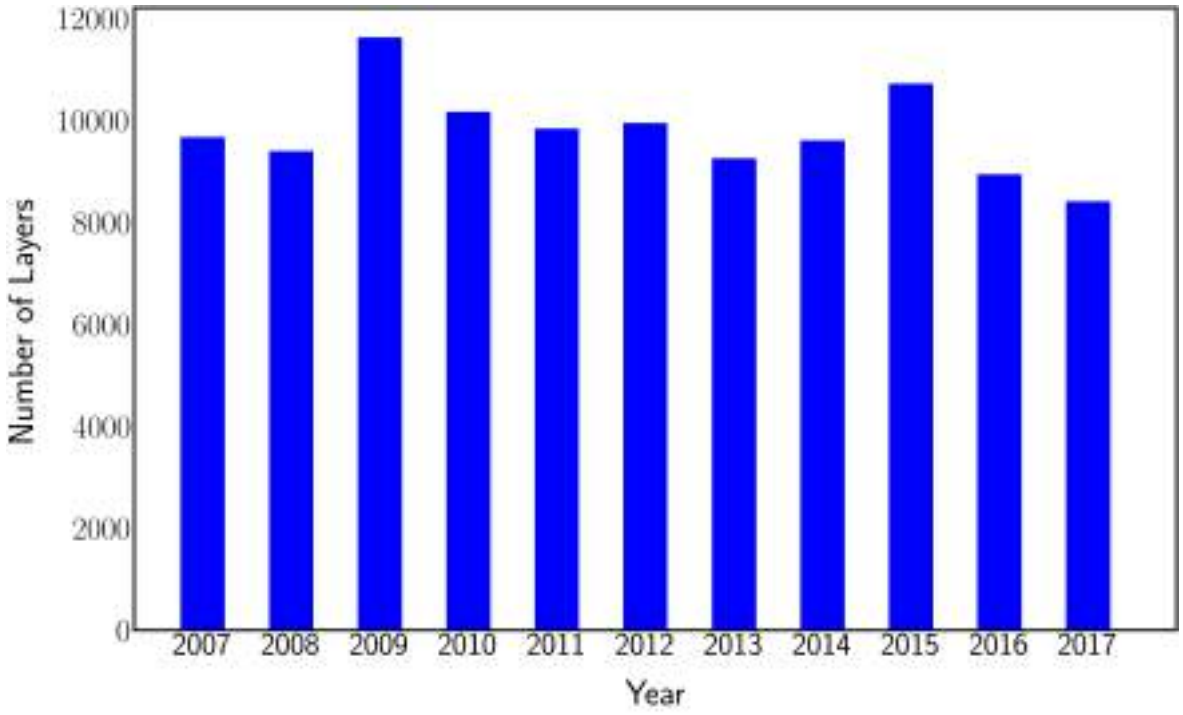

Source: Author

Figure 25 – Total number of cirrus cloud layers detect per year.

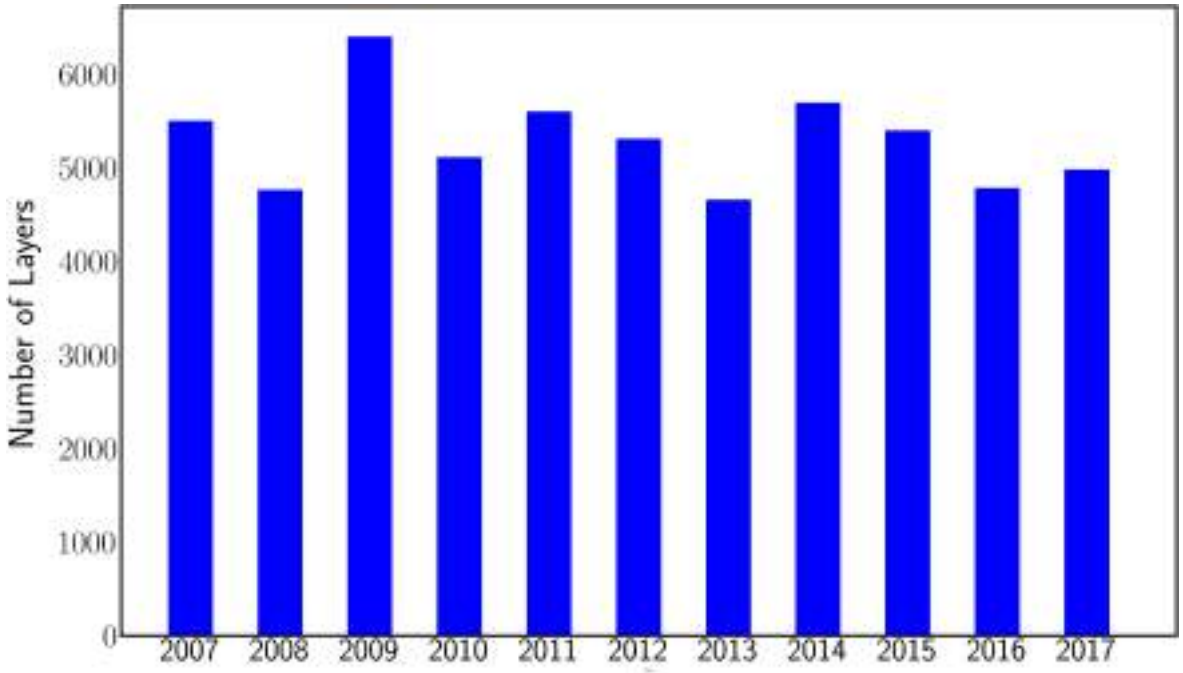

Source: Author

Figure 26 – Frequency of occurrence of all cloud types throughout the years.

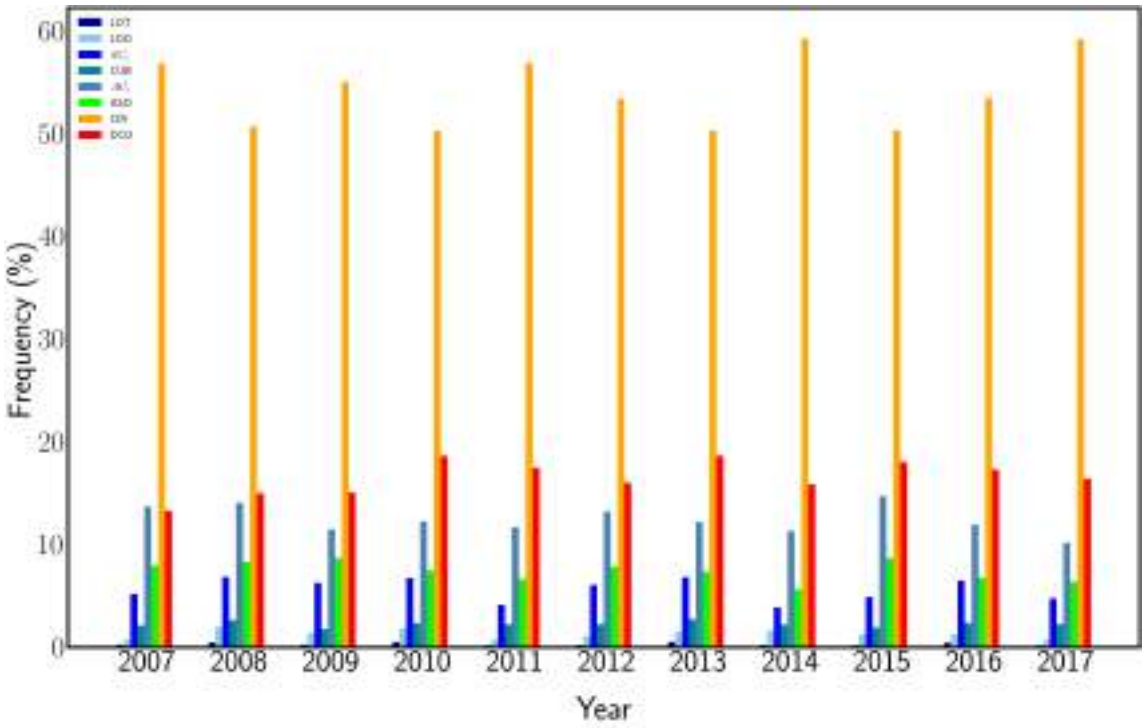

Source: Author

Figure 27 – Yearly distribution of cirrus base heights for the whole period of analysis.

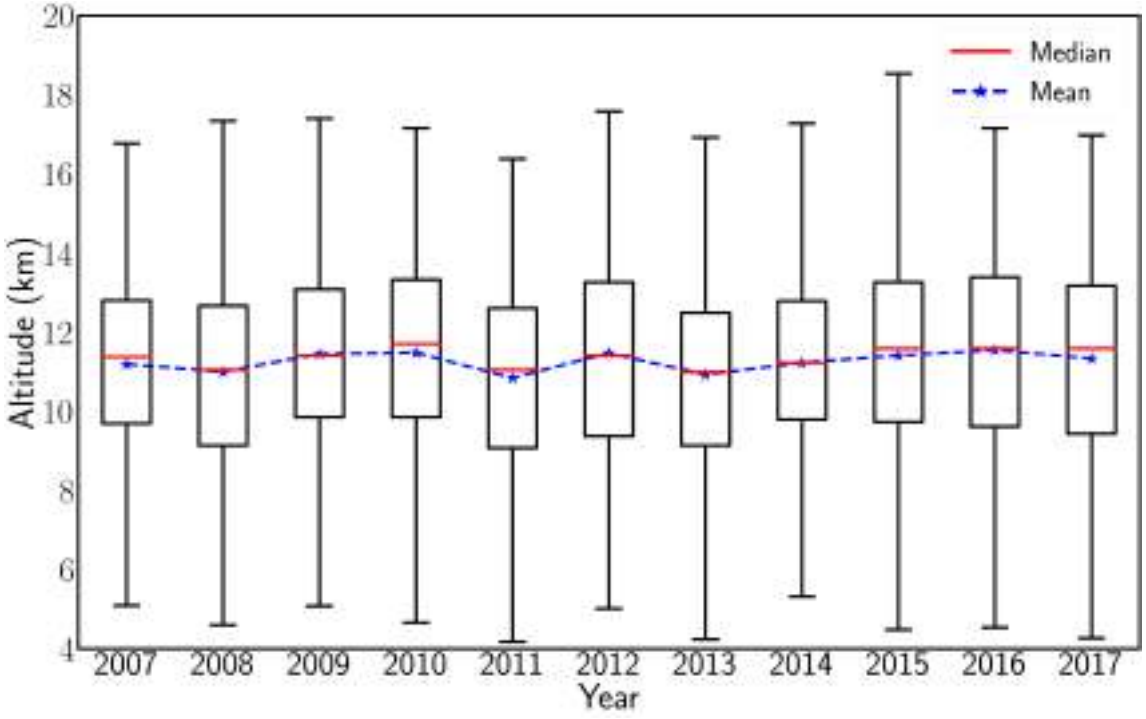

Source: Author

Figure 28 – Yearly distribution of cirrus top heights for the whole period of analysis.

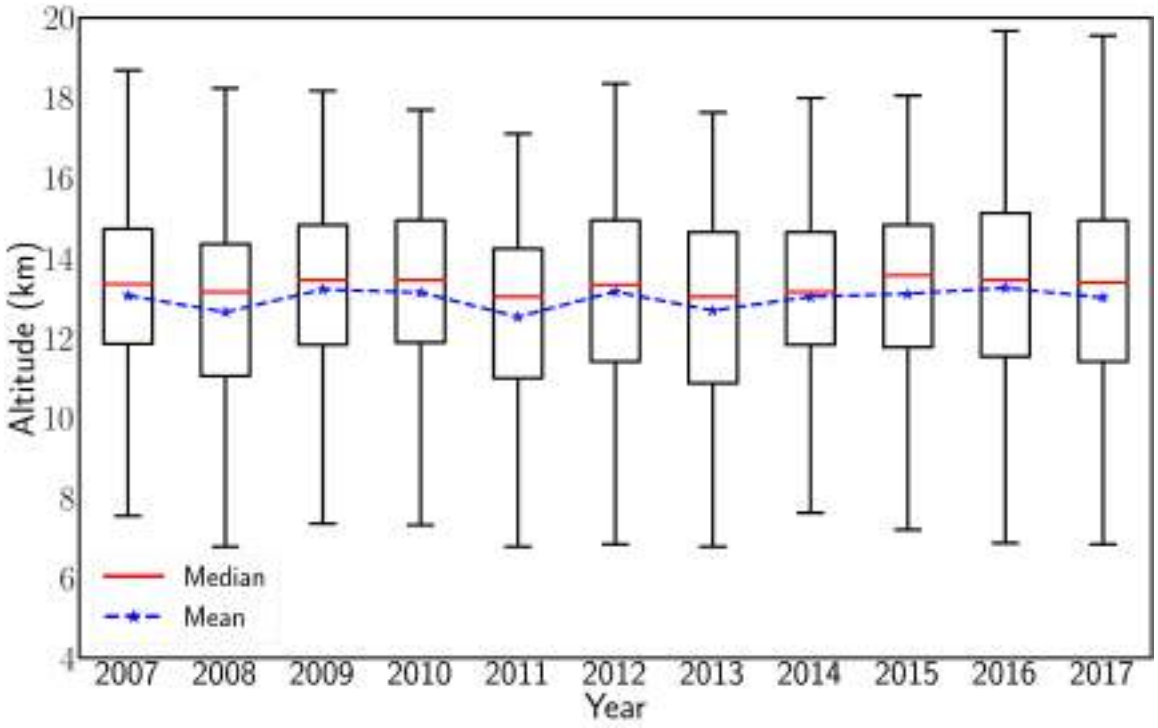

Source: Author

Figure 29 – Yearly distribution of cirrus thickness.

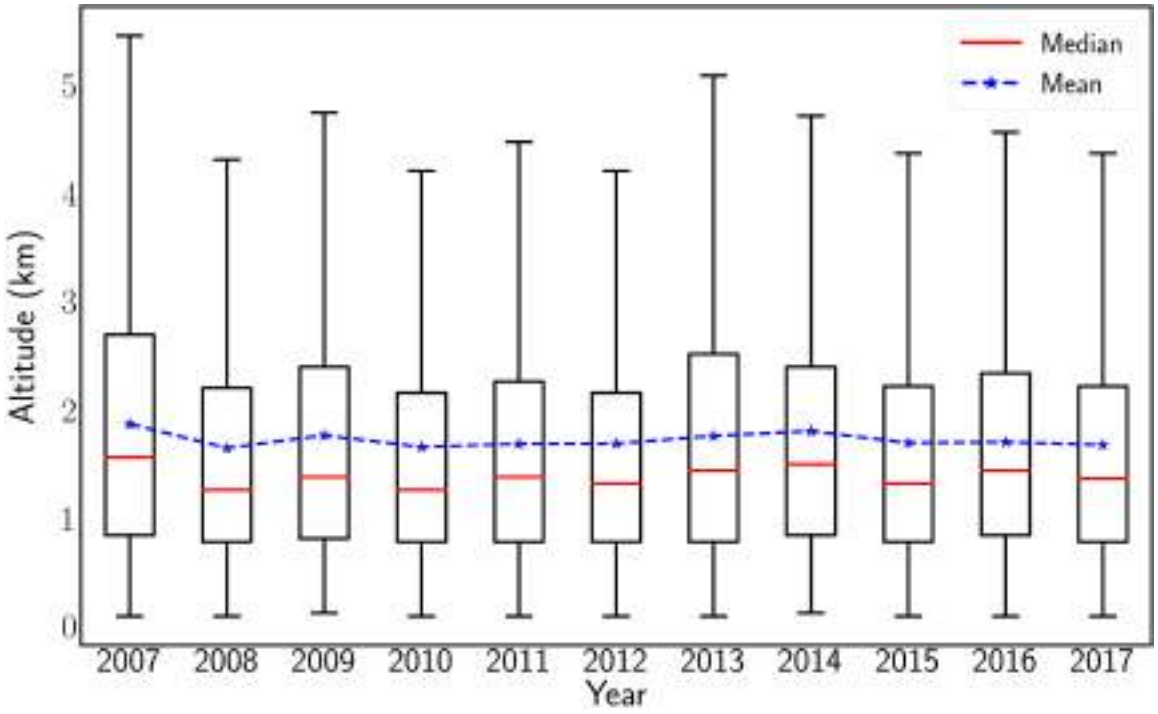

Source: Author

Figure 30 – Yearly distribution of the cirrus bases temperature.

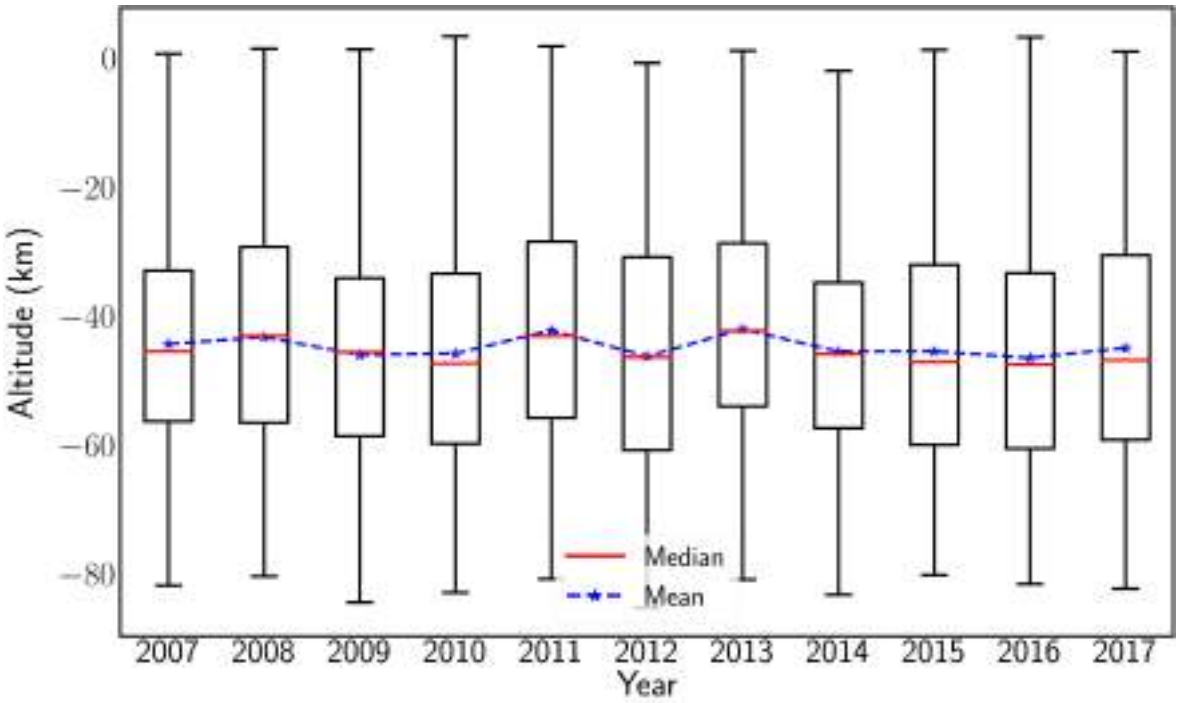

Source: Author

Figure 31 – Yearly distribution of the cirrus tops temperature.

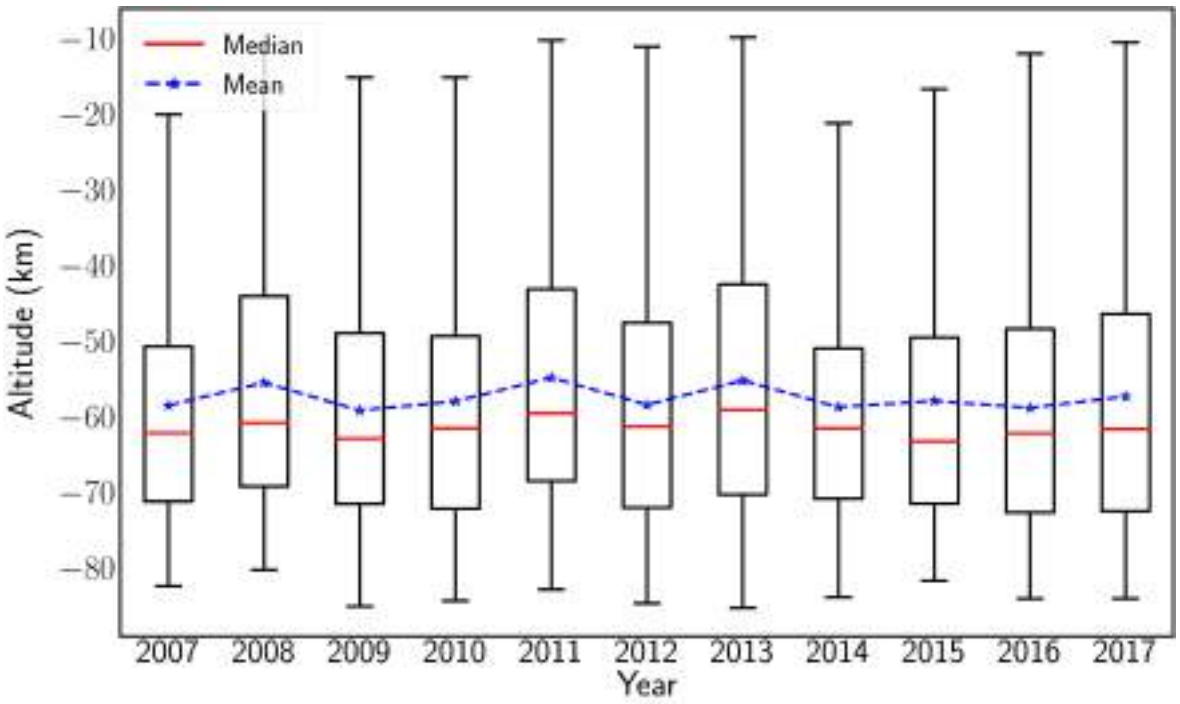

Source: Author

Figure 32 – Yearly frequency of clouds occurrence in the atmosphere with respect to height.

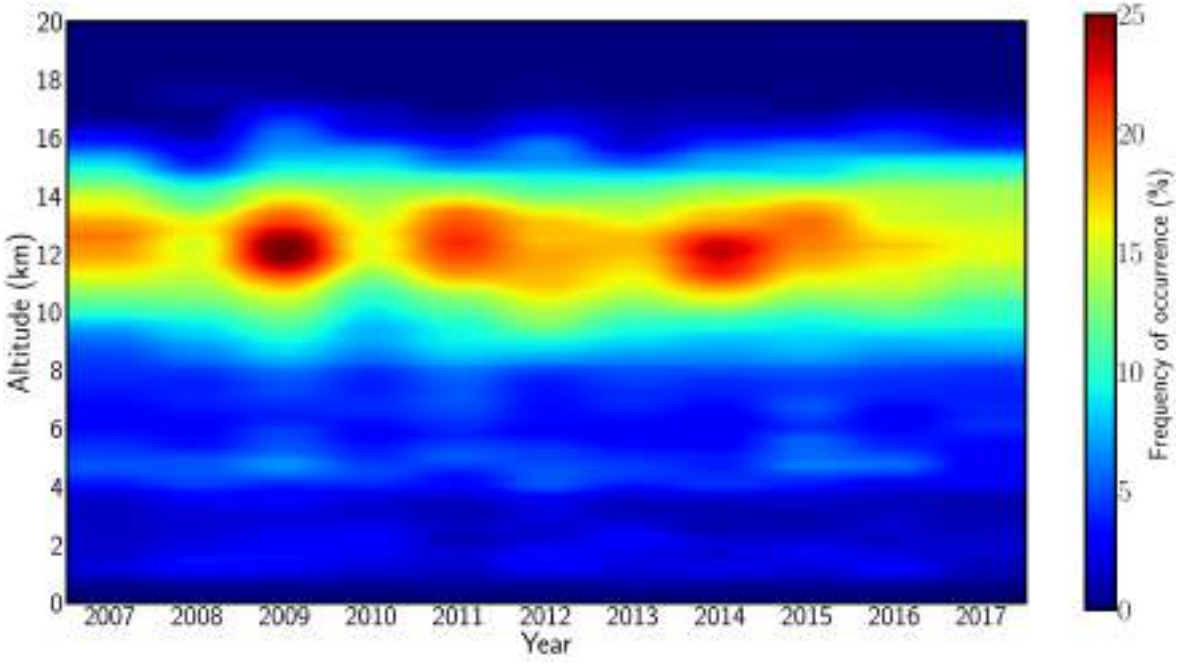

Source: Author

Figure 33 – Yearly frequency of cirrus occurrence in the atmosphere with respect to height.

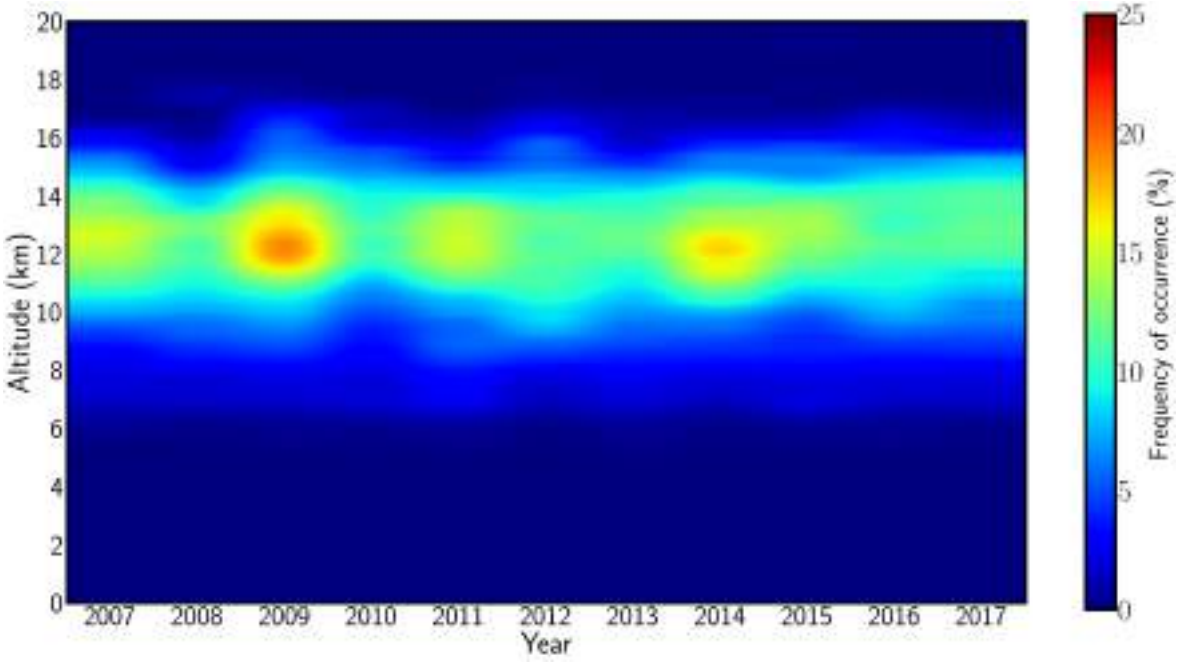

Source: Author

Figure 34 – Yearly frequency of DCO occurrence in the atmosphere with respect to height.

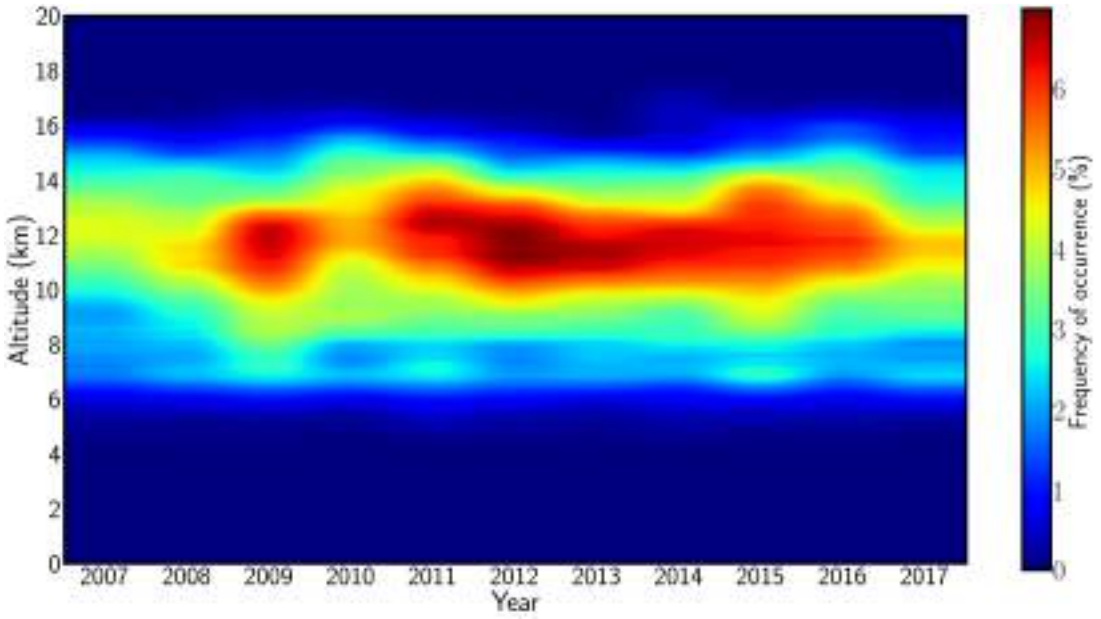

Source: Author

5.3 Monthly distribution

Figure 35 shows the frequency of occurrence of clouds over multiple years, calculated by selecting the total clouds detected in each month over the 11-year period and dividing it by the total clouds detected for that month. Figures 36 and 37 show the distribution of base and top heights, respectively, for cirrus clouds, separated by the months of the year. The distribution of cirrus thickness is shown in Figure 38, which is calculated as the difference between the top and base heights of the clouds. Figure 39 illustrates the monthly distribution of cirrus base temperatures, while Figure 40 shows the monthly distribution of cirrus top temperatures.

Finally, to determine the monthly frequency of cloud occurrence with respect to altitude, the total number of clouds detected at a given height was divided by the number of times the CALIPSO satellite passed over the region of interest. The resulting data is presented in Figure 41. Similarly, the monthly frequency of occurrence of cirrus clouds with respect to altitude can be determined by selecting only cirrus clouds and dividing them by the total passages of CALIPSO per month, as shown in Figure 42. To compare with cirrus formation, the distribution of DCO with respect to height is shown in Figure 43.

Figure 35 – Multiyear monthly frequency of occurrence of all cloud types.

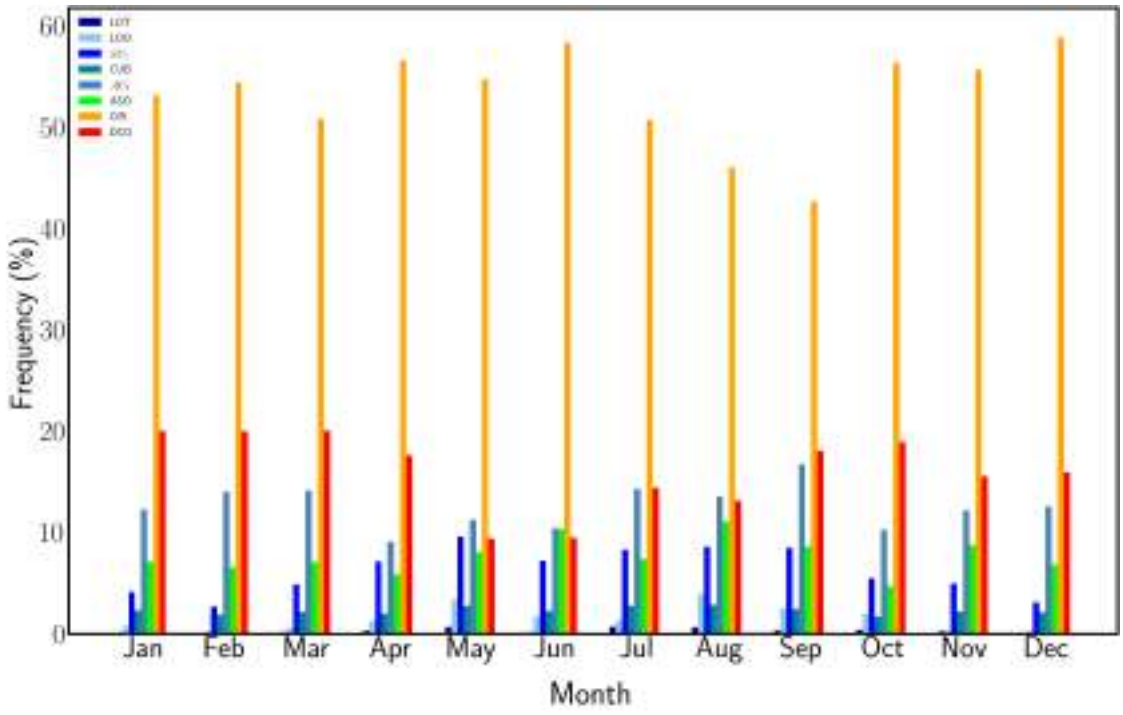

Source: Author

Figure 36 – Multiyear monthly distribution of cirrus base height.

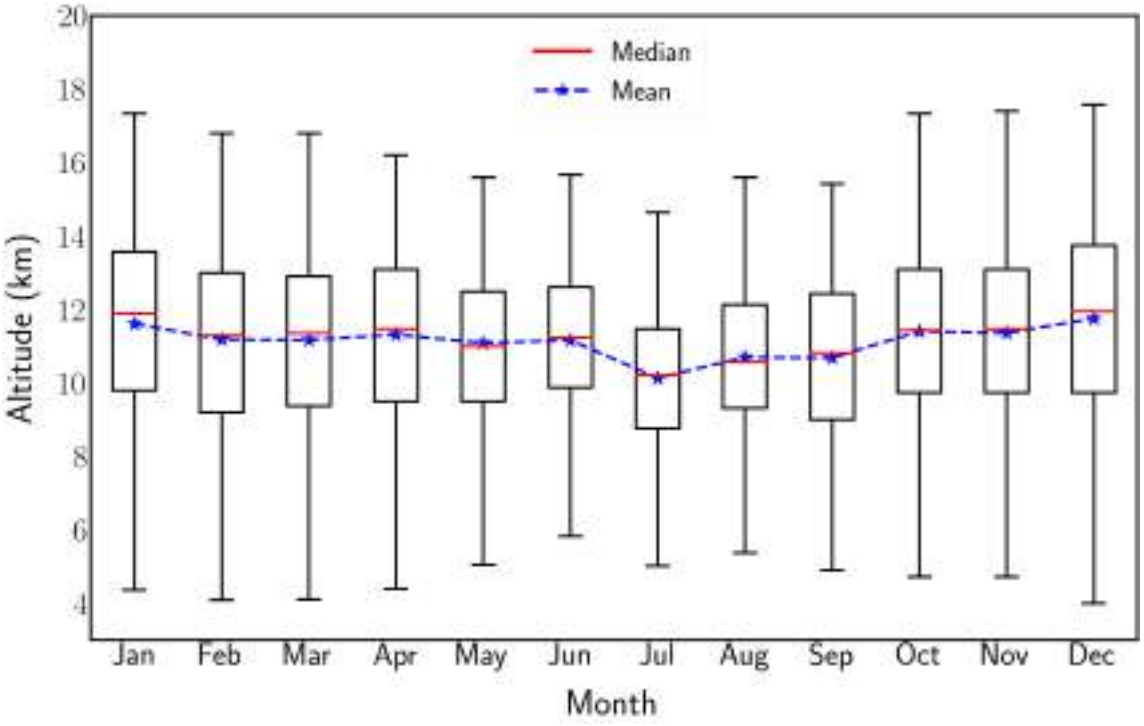

Source: Author

Figure 37 – Multiyear monthly distribution of cirrus top height.

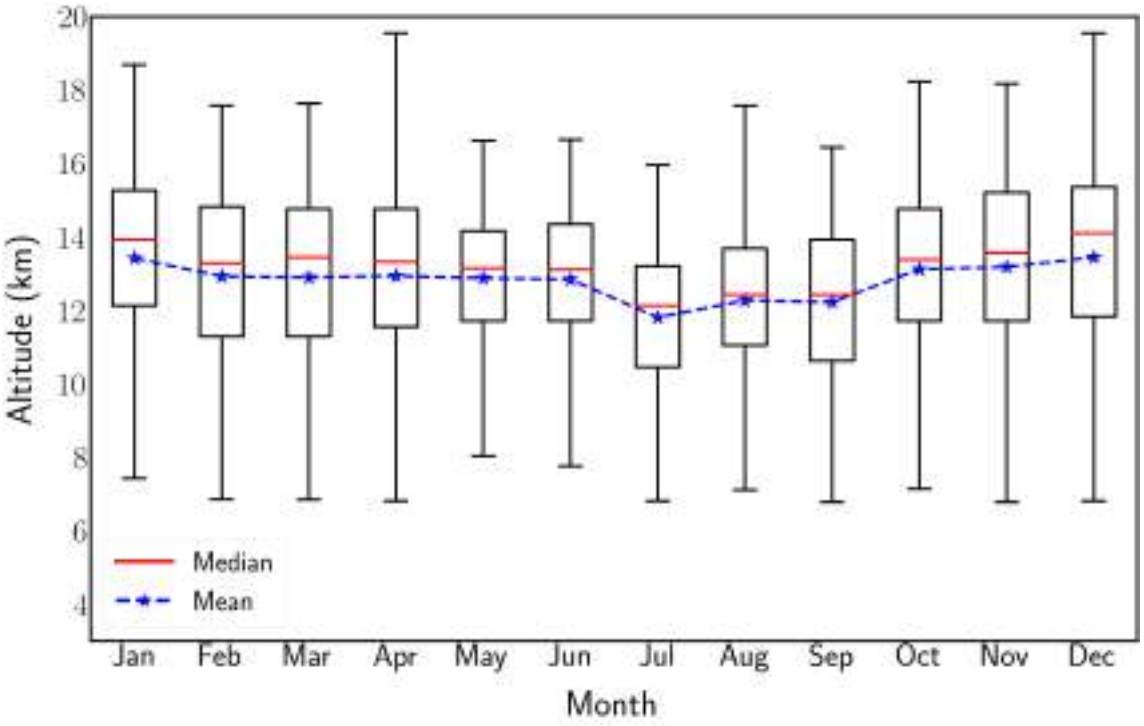

Source: Author

Figure 38 – Multiyear monthly distribution of cirrus thickness.

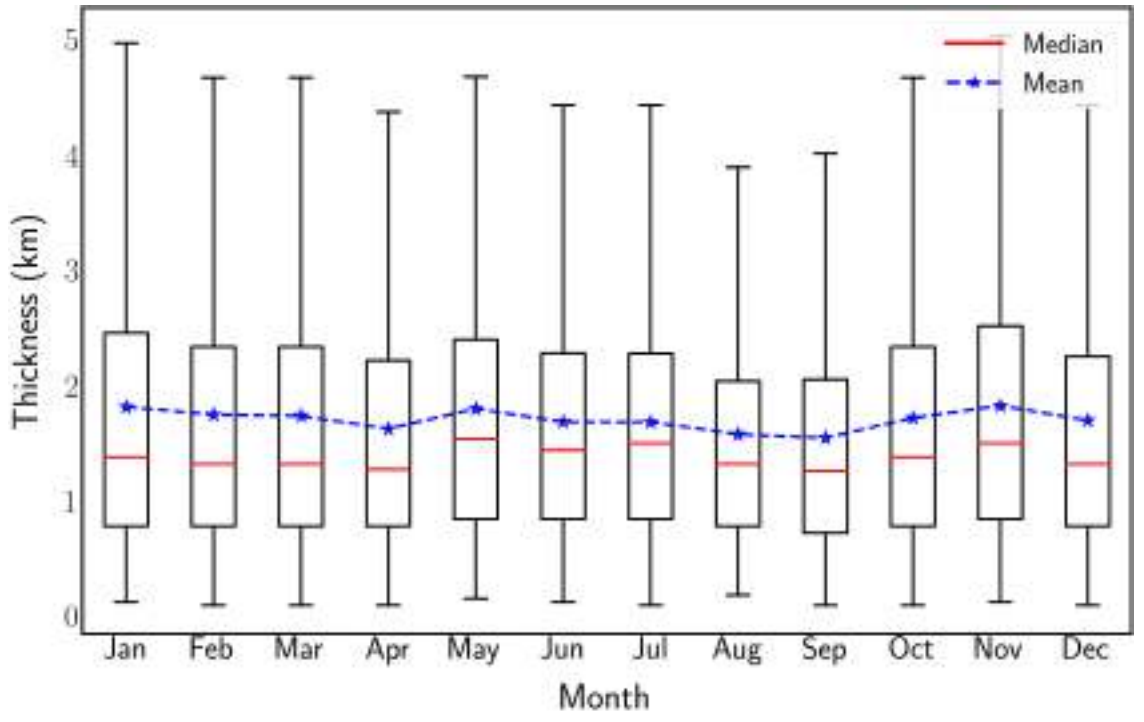

Source: Author

Figure 39 – Multiyear monthly distribution of cirrus base temperature.

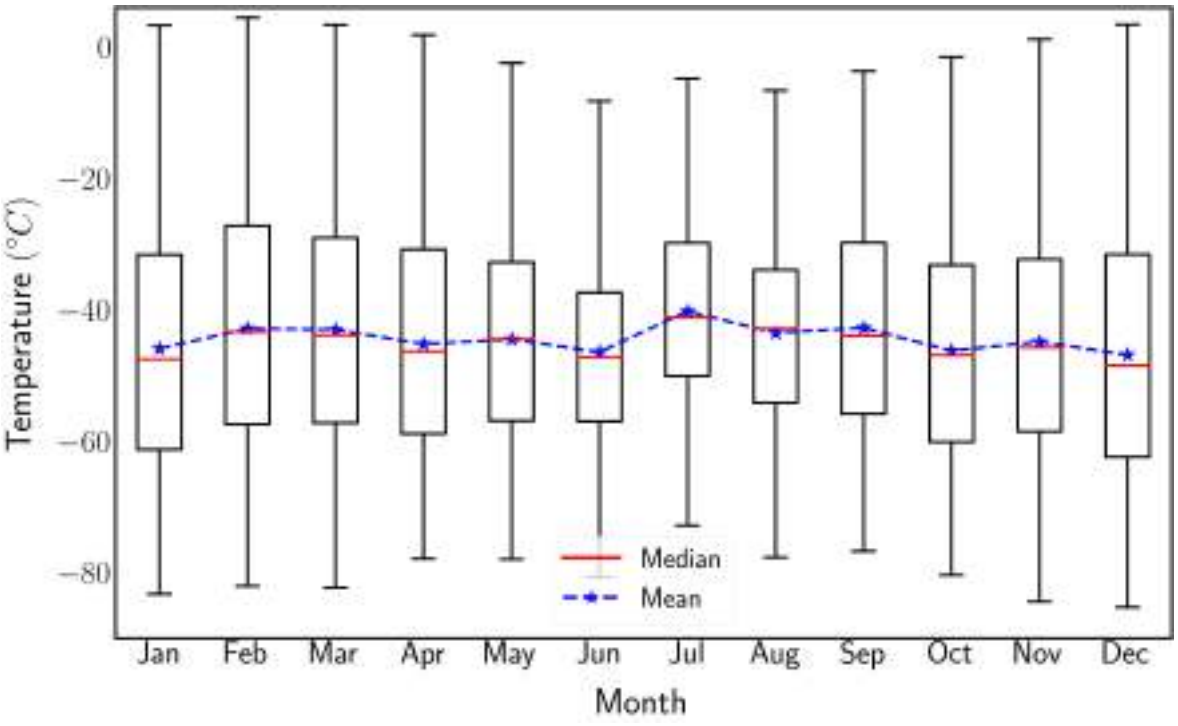

Source: Author

Figure 40 – Multiyear monthly distribution of cirrus top temperature.

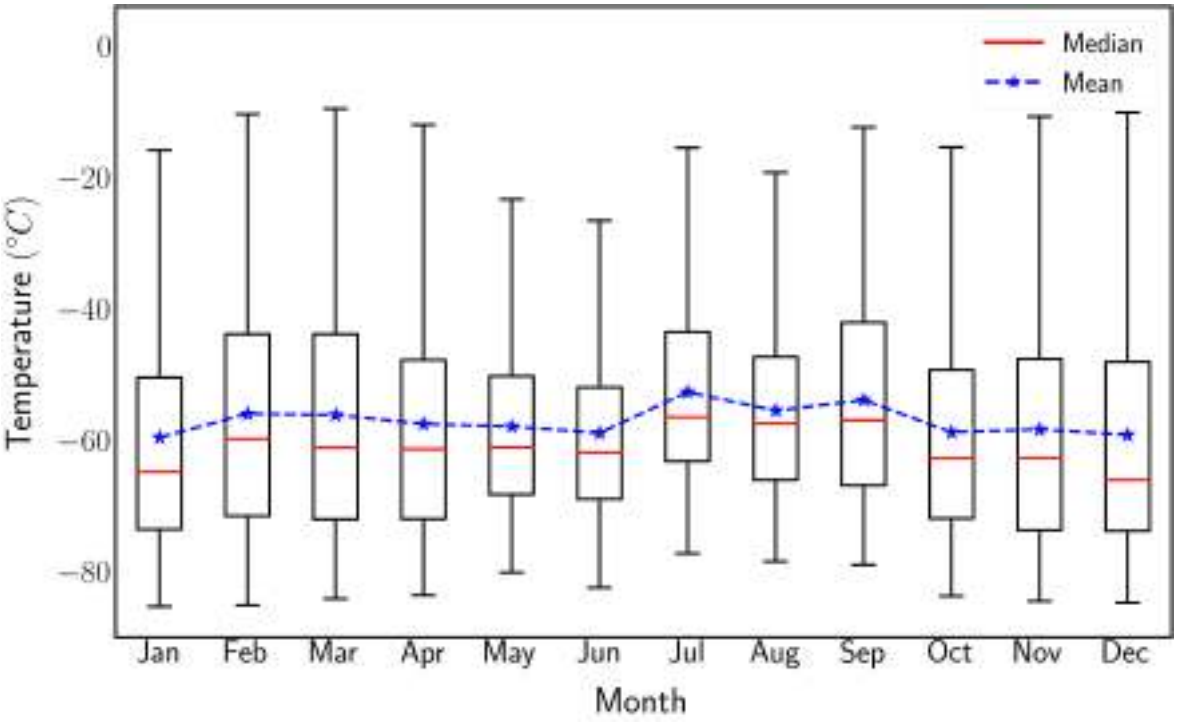

Source: Author

Figure 41 – Multiyear monthly frequency of clouds occurrence in the atmosphere with respect to height.

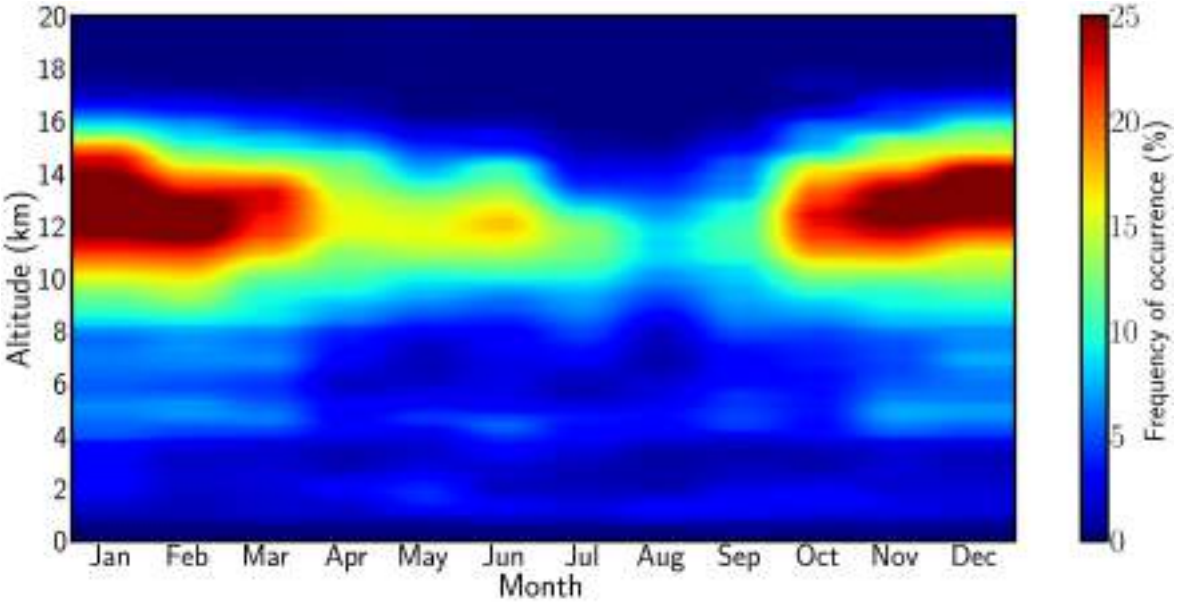

Source: Author

Figure 42 – Multiyear monthly frequency of cirrus occurrence in the atmosphere with respect to height.

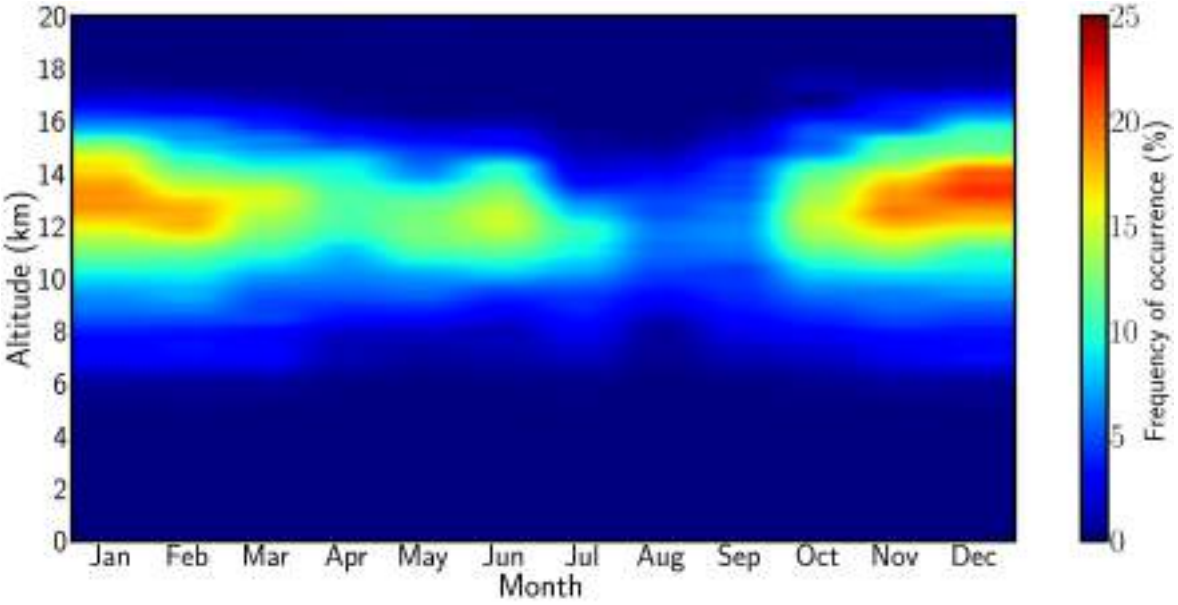

Source: Author

Figure 43 – Multiyear monthly frequency of DCO occurrence in the atmosphere with respect to height.

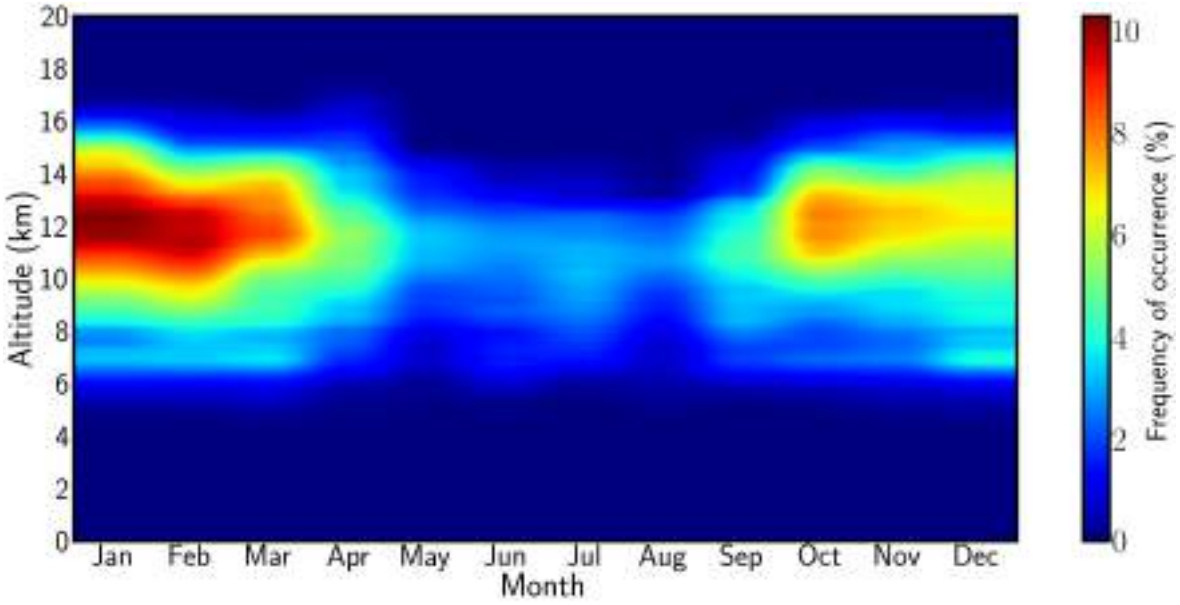

Source: Author

5.4 Cirrus cloud optical depth

We obtained the COD from the "Feature Optical Depth"product, Figure 44 shows the COD distribution for each type of cloud. For cirrus clouds, we analyzed the yearly distribution of COD, and the results are shown in Figures 45, 46, and 47. The classification was carried out following the criterion proposed by Sassen & Cho (1992), as discussed earlier. We also investigated the monthly distribution of COD for cirrus clouds, and the results are presented in Figures 49, 50, and 51.

Figure 44 – Histogram distribution of COD for all cloud types.

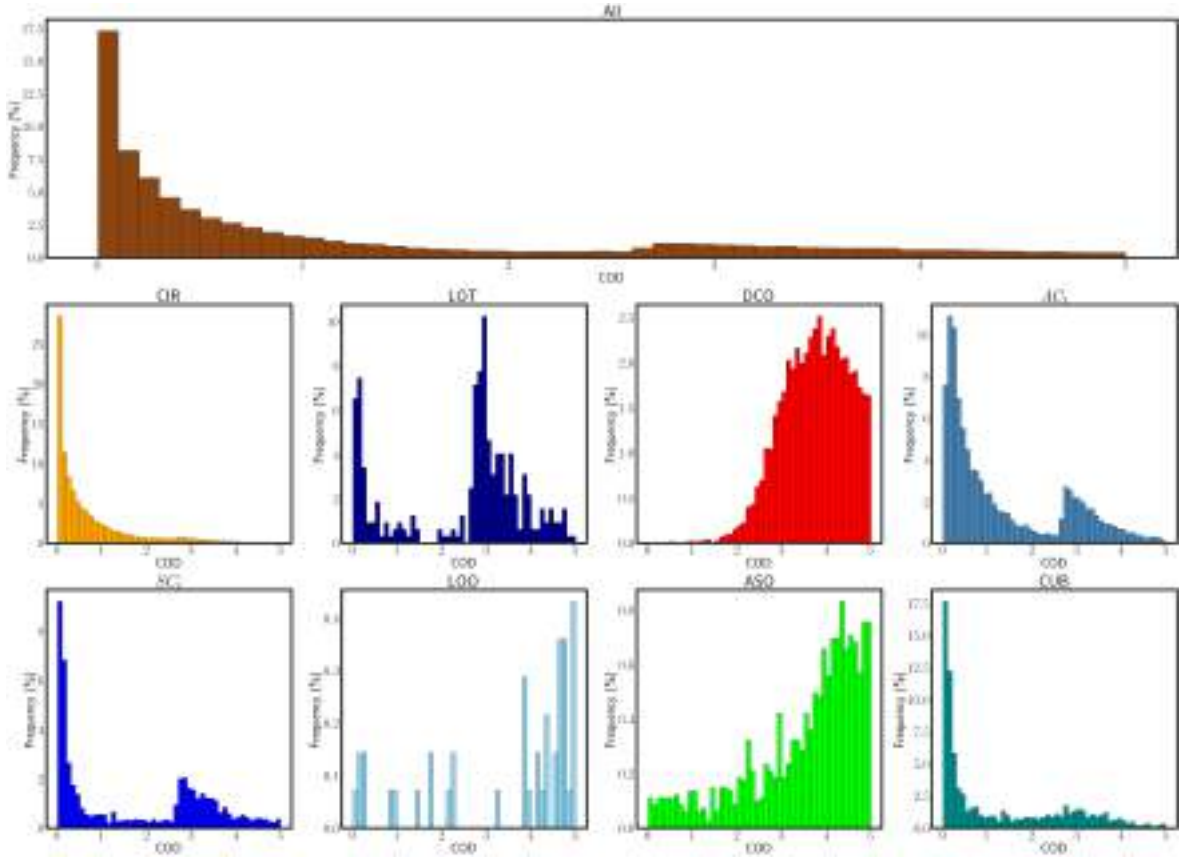

Source: Author

Figure 45 – Yearly distribution of subvisible cirrus COD.

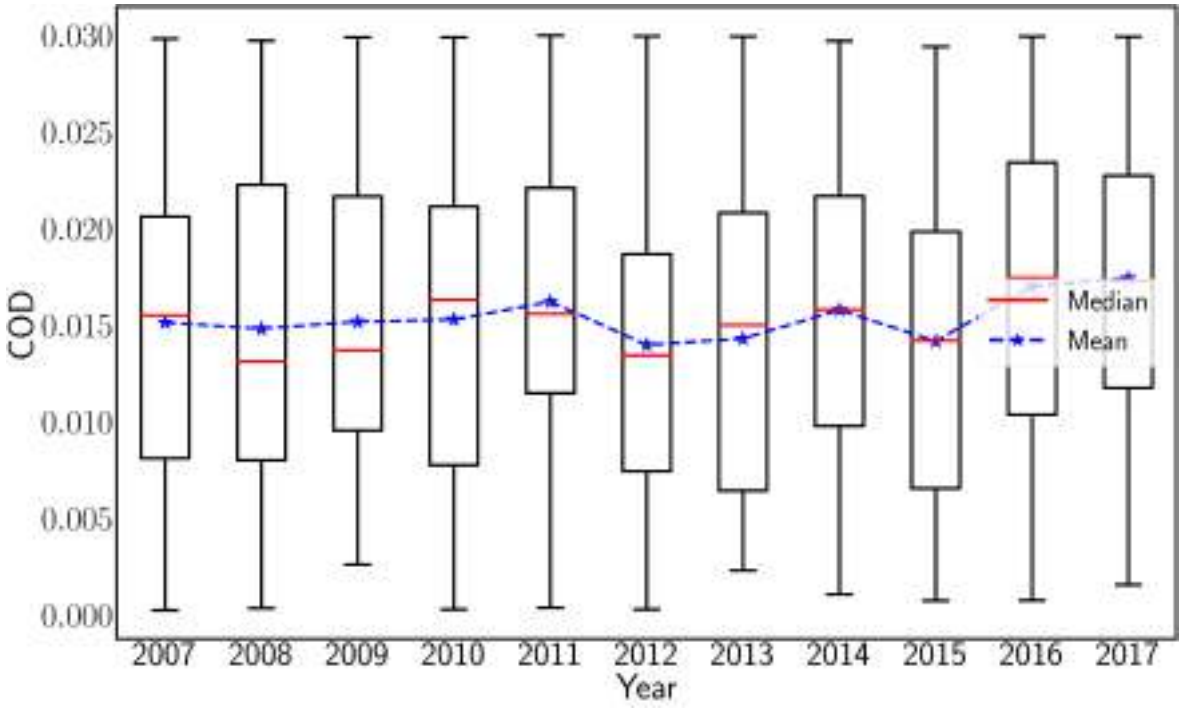

Source: Author

Figure 46 – Yearly distribution of thin cirrus COD.

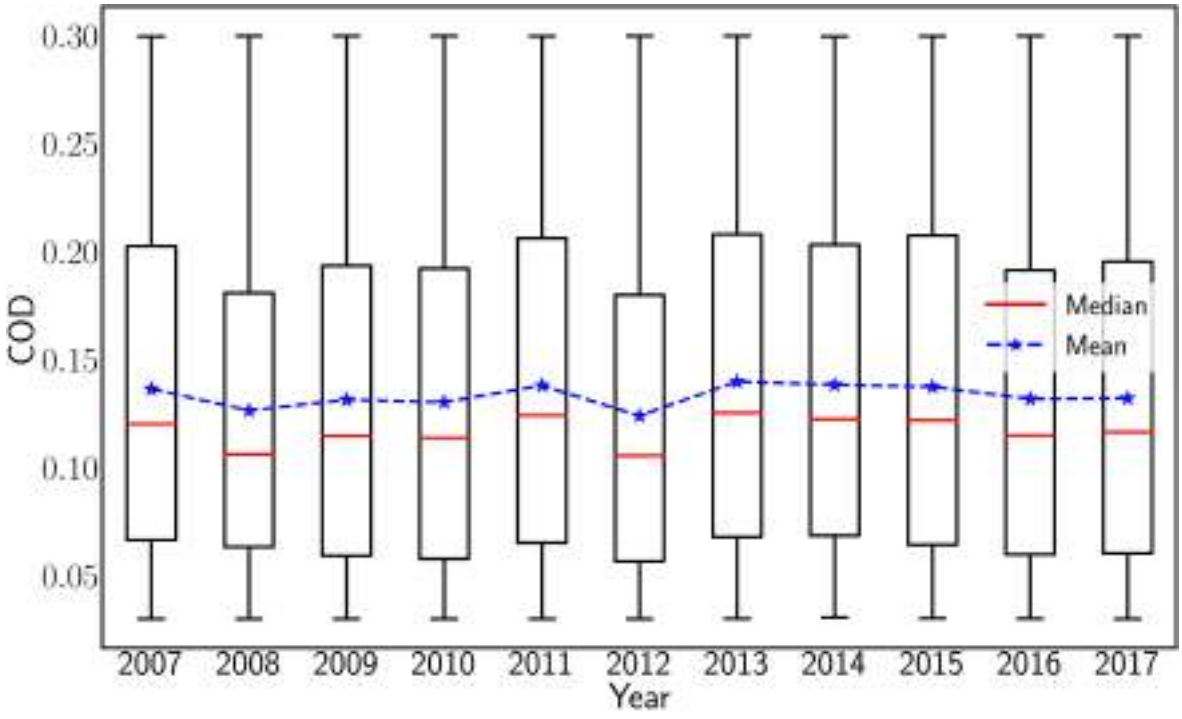

Source: Author

Figure 47 – Yearly distribution of thick cirrus COD.

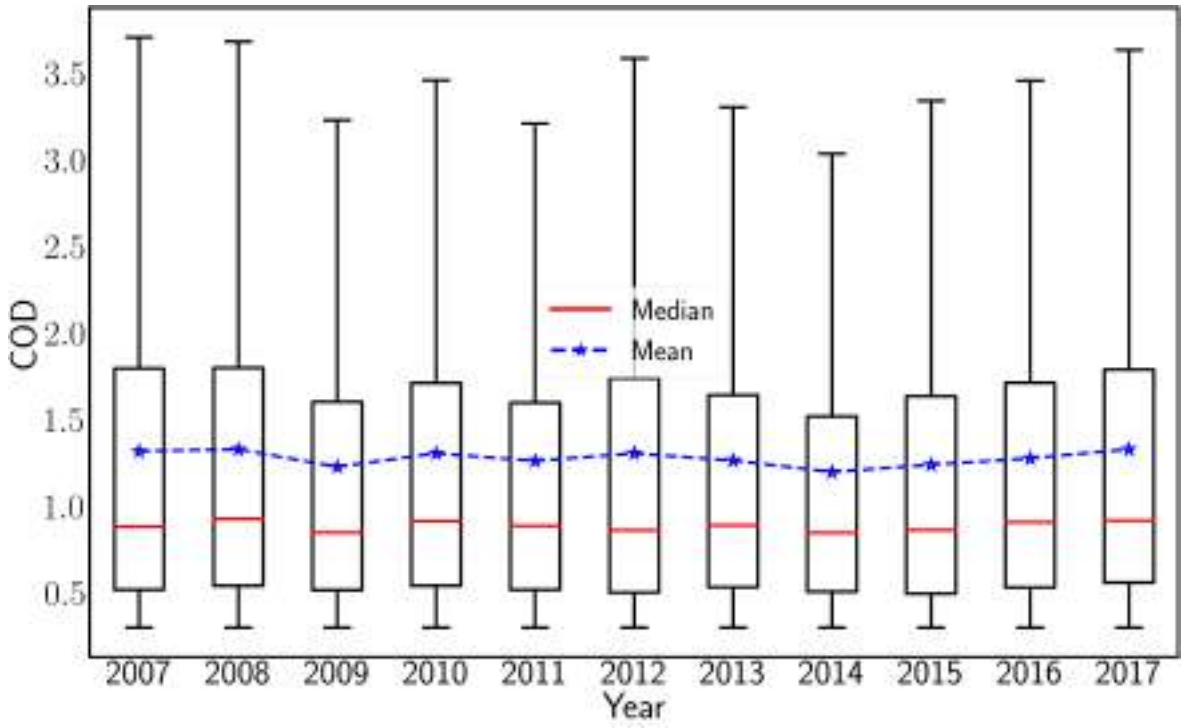

Source: Author

Figure 48 – Frequency of occurrence of COD for all three types of cirrus for each year.

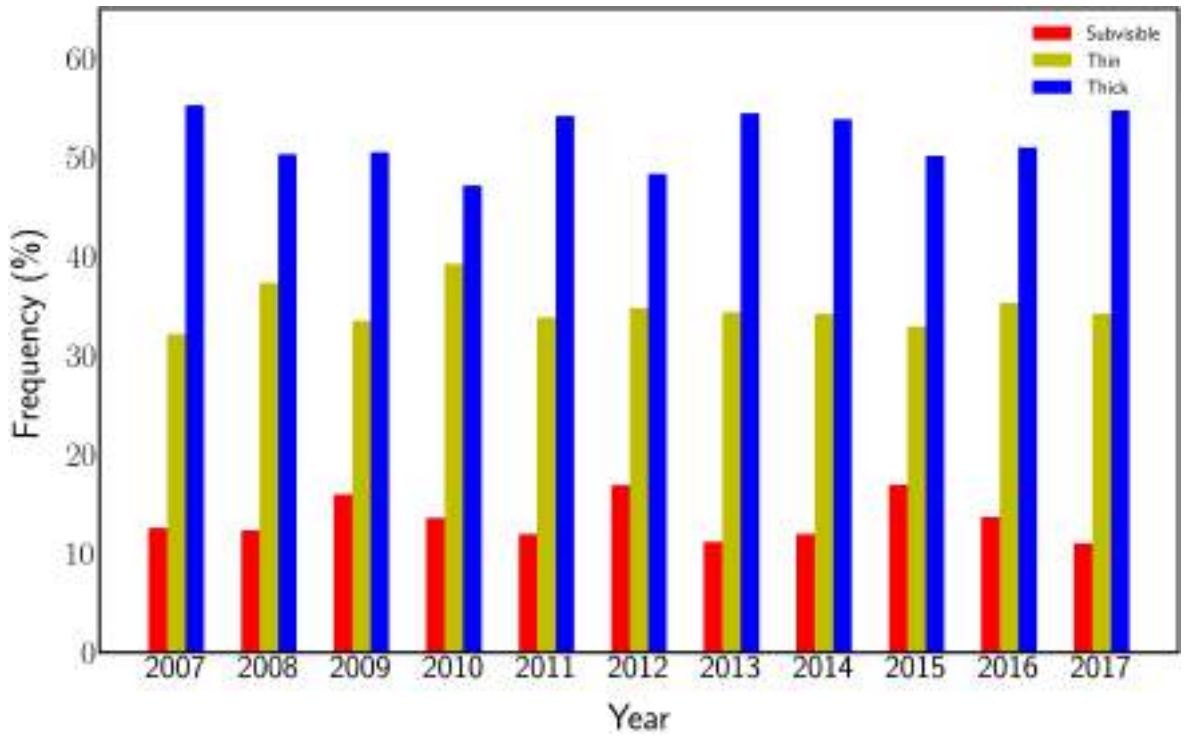

Source: Author

Figure 49 – Multiyear monthly distribution of subvisible cirrus COD.

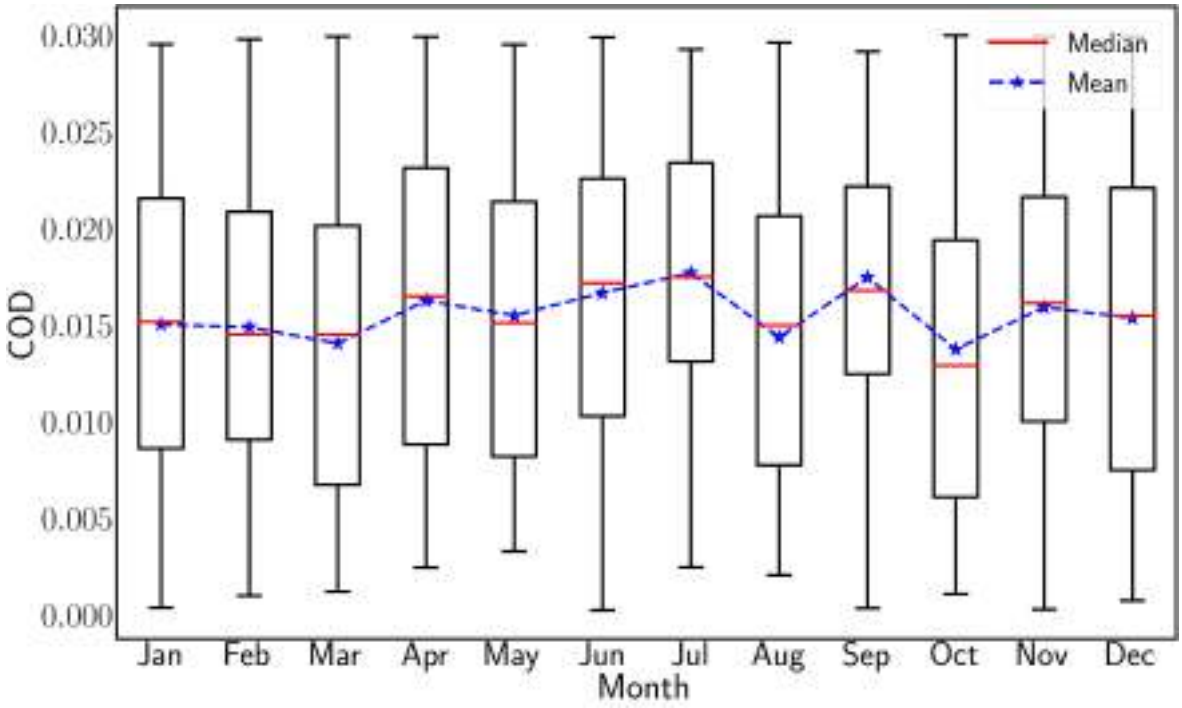

Source: Author

Figure 50 – Multiyear monthly distribution of thin cirrus COD.

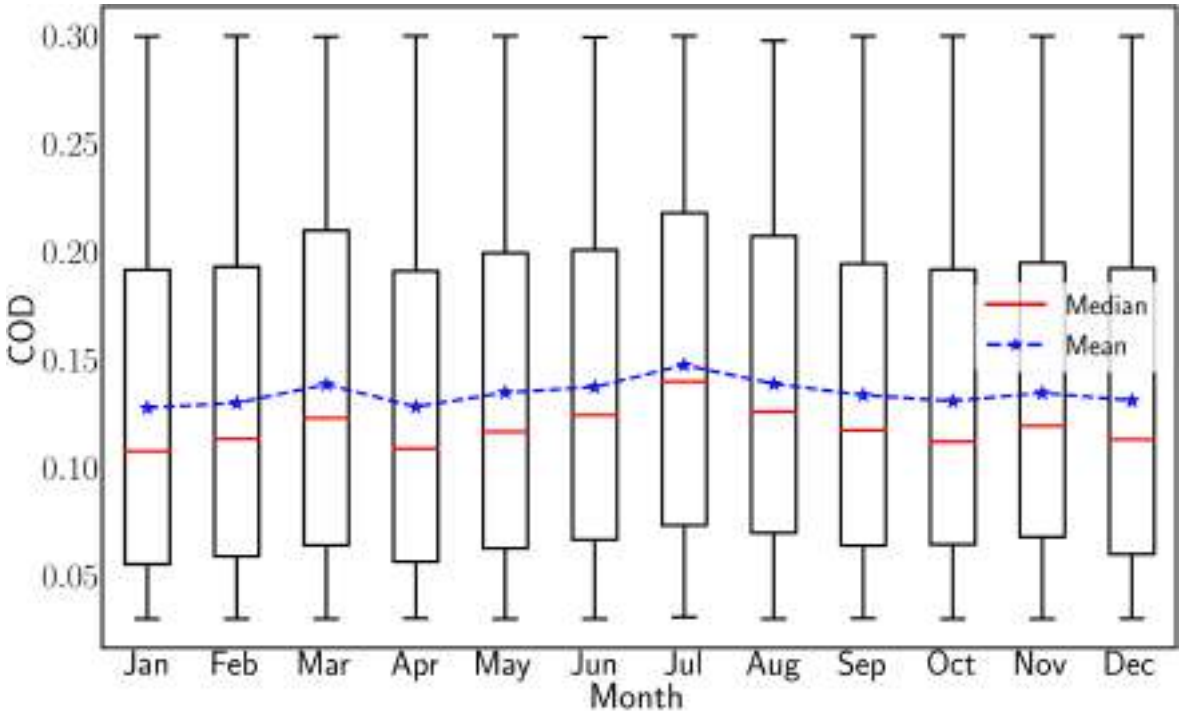

Source: Author

Figure 51 – Multiyear monthly distribution of thick cirrus COD.

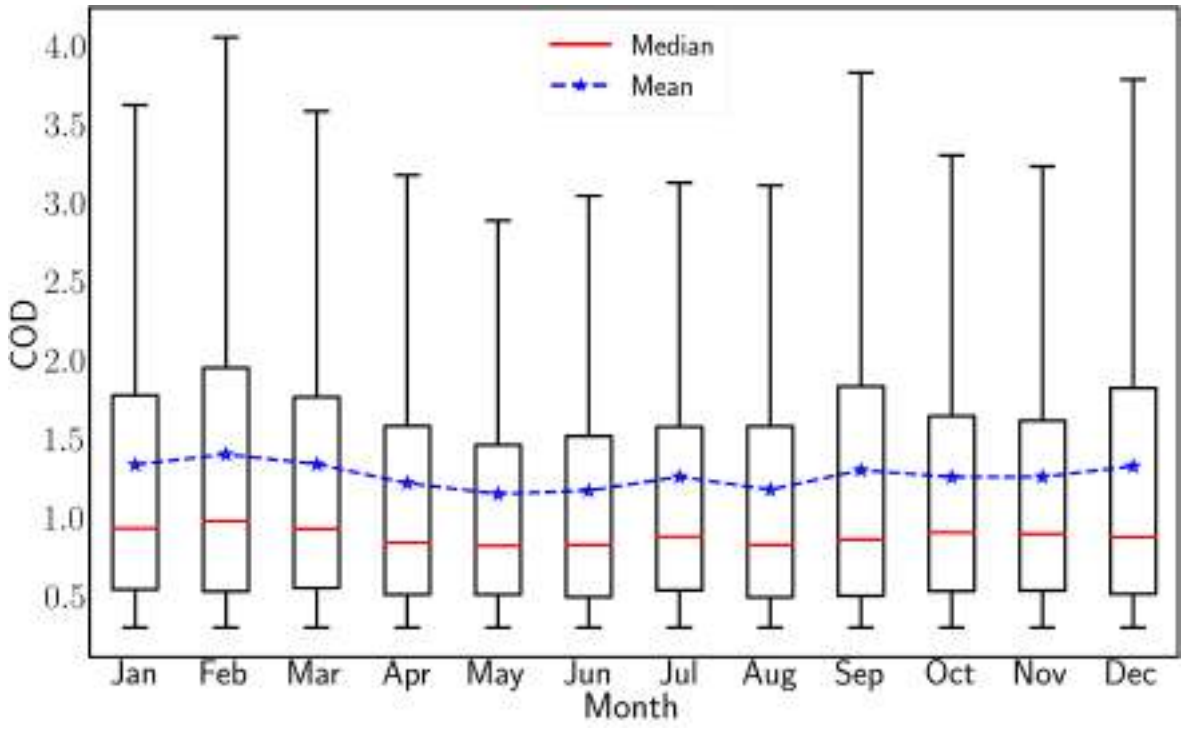

Source: Author

Figure 52 – Frequency of occurrence of COD for all three types of cirrus for each month.

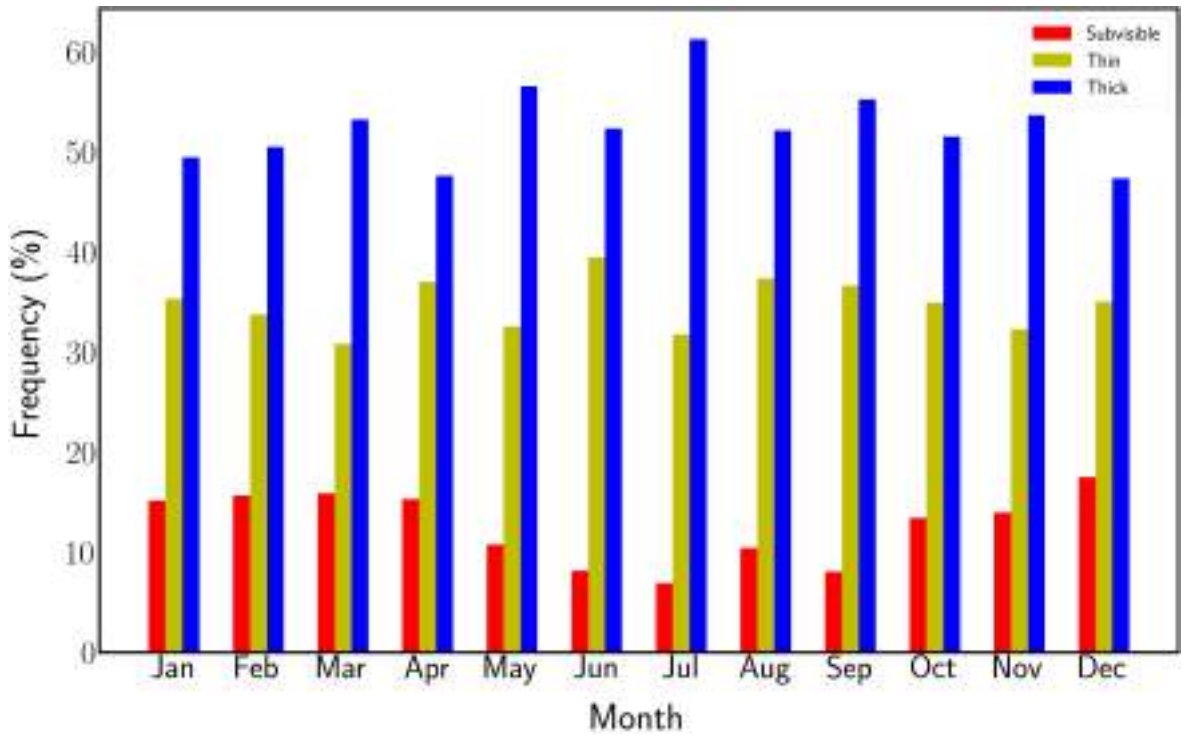

Source: Author

6 Discussion

We can see in Figure 23 that the average frequency of low-energy shots is less than 5% for the years before 2017, but from 2017 onward the impact of SAA on CALIPSO measurements grows exponentially reaching more than 80% in 2020. Due to this loss of data, measurements performed by CALIPSO that were affected by the SAA and have a QA below "high" were not considered. Since 2018 there was no cloud detection with high QA so those years were not considered in the analysis.

Figure 26 shows the yearly frequency of occurrence for each cloud type, revealing that cirrus is the most common cloud type, with a frequency of occurrence above 50% in all eleven years. DCO clouds are the second most common type, with values ranging from 12.5% to 18%, followed by AC_t with values between 10% and 15%. The other cloud types have a distribution below 7.5%, with LOT being the least frequent with less than 0.5% frequency of occurrence.

Regarding the occurrence of clouds at different altitudes, we can observe from Figure 32 that there is a maximum frequency of occurrence between 10 and 15 km, which can vary from year to year, with some years reaching 25% of frequency of occurrence and others having lower values around 15%. Doing the same analysis but only for cirrus (Figure 33), we see that cirrus starts to form at altitudes above 7 km, and the most frequent region of occurrence is between 11 and 14 km. This pattern is similar for all eleven years. The only difference is at 12-13 km where in some years the frequency of occurrence increased. In particular, there was a biennial oscillation between 2007 and 2012, followed by a decrease in the maximum values in 2013, and then an increase in 2014.

Looking at the measured DCO height in Figure 34 we see that this type of cloud is detected in similar altitudes to cirrus, meaning that they correlate during the formation process. This is a piece of evidence that shows how the formation of cirrus is affected by convection and part of the cirrus present over the state is

formed due to an anvil, as expected in a tropical region. This is also observed when comparing Figure 42 and 43, when it is on the rainy season (Dec-Mar) the frequency of occurrence of cirrus and DCO increases, and their peak of occurrence is in the same range around 11 to 15 km.

The distribution of cloud bases over the years is similar, with a range between 10 and 13 km and a median value varying between 11 and 12 km (Figure 27). In Figure 28 we see that cloud tops range from 12 to 15 km, and the median top height varies between 13 and 14 km. The thickness of cirrus clouds in Figure 29 ranges from 0.5 to 2.5 km, with a median value of approximately 1.4 km in all years. The temperatures of cloud bases consistently fall within the range of -60 to -30 ◦ C (Figure 30), with the median base temperatures varying between -50 and -40 ◦ C over the same period. Cloud top temperatures in Figure 31, exhibit a consistent range of -60 to -30 ◦ C, with the median temperature varying between -50 and -40 ◦ C over the years.

When looking at the distribution of cloud types by month represented in Figure 35, cirrus is the most frequent cloud type, with a frequency of occurrence above 50% in almost every month. In the months between July and September, this frequency gets lower reaching 40%. DCO clouds reach 20% frequency of occurrence in rainy months when get as low as 10% months of less rain occurrence. The physical properties of cirrus did not change much from month to month (Figures 36 and 37) showing only a decrease in months of winter (Jul-Sept), this decrease can be of almost 2 km from June to July. The temperature of the base and top increases when cirrus formed at lower altitudes since the temperature is higher at lower altitudes.

Analyzing the distribution of the COD of clouds (Figure 44), we can observe that more than half of the clouds have a COD below 1, with the highest occurrence at 0.1 with a frequency of occurrence of 17%. Among the different cloud types, cirrus clouds have the lowest COD, with almost half of the frequency of occurrence less than 0.3. The CUb and ACt types also have a high-frequency distribution at COD lower than 0.3, indicating that they can be confused with cirrus if they form in higher altitudes. The other types of clouds have a greater distribution for COD above 0.3.

The analysis of the opacity of cirrus following the from Sassen & Cho (1992) showed that the most common type of cirrus is thick with a frequency of occurrence of more than 50% followed by thin cirrus type with 30% of occurrence and

the less present is the subvisible with 15% (Figures 45, 46 and 47). The seasonal distribution of cirrus types, represented in Figures 49, 50 and 51 follows the same pattern, but in months from May to September there is a drop of 5% in the occurrence.

Conclusion

Eleven years of level 2 data from CALIPSO/CALIOP was used to investigate the characteristics of cirrus clouds over the state of São Paulo, Brazil. The results of this study have shown that cirrus clouds are the most prevalent type of cloud in the region in comparison with the seven types used by the VFM product. The frequency of occurrence of cirrus is greater than 50% in all of those years between 2007 and 2017. In comparison, the second most present cloud showed a frequency of less than 20%, this shows how abundant cirrus clouds are in the region.

By analyzing the vertical characteristics of cirrus clouds, it was possible to observe that they typically form at altitudes above 8 km and below 16 km, with the most frequent occurrence in altitudes between 10 and 14 km. Additionally, the study confirmed that cirrus clouds are relatively thin, with an average thickness of approximately 1.4 km. This information is important because it provides insight into the physical properties of cirrus clouds, which can impact the overall radiative budget of the Earth's atmosphere.

With regards to temperature, the data showed that cirrus clouds form at extremely low temperatures, typically around $-50°C$, which is consistent over the years. This is because cirrus clouds are usually found at higher altitudes where the temperature of the ambient is very low. The study also confirmed that cirrus is optically a thin type of cloud, with the COD of cirrus clouds being below 1 for 80% of the observed data.

The seasonal frequency of occurrence showed that cirrus clouds were present in approximately 15% of the observations during most of the year, with peaks of 20% of frequency occurring between the months of November and February. The lowest frequency of cirrus cloud occurrence was observed in August and September. The frequency of cirrus cloud occurrence was also analyzed over the entire eleven-year period, revealing that the frequency oscillated between 12% and 15%, with

2009 being the year with the highest occurrence, reaching almost 20% at 12-14 km. The seasonal analysis of cirrus was useful to observe the correlation between the formation of cirrus with DCO clouds as expected for tropical regions.

The optical properties of cirrus showed that cirrus is the thinnest cloud type with the COD most frequently below 1. The analysis of cirrus COD showed that thick cirrus is the most common type with a frequency of occurrence superior to 45% for every year and month. This result agrees with the case study of Cordoba-Jabonero et al. (2017), where the measurement from CALIPSO and a ground-based lidar detected more thick cirrus than the other two types. The seasonal distribution of cirrus COD showed that only subvisible cirrus changed, with a drop in the frequency of occurrence between May and September.

The physical and optical properties of cirrus clouds obtained in this study can provide valuable insights into the interaction between cirrus clouds and the radiative budget, as well as contribute to the improvement of climate models, and contribute to a better understanding of climate change. In addition, the observed seasonal distribution of cirrus clouds offers an opportunity for further investigations into the underlying mechanisms of cirrus cloud formation and distribution over the state, which could further enhance our understanding of atmospheric processes.

References

ABSHIRE, J. B.; SUN, X.; RIRIS, H.; SIROTA, J. M.; MCGARRY, J. F.; PALM, S.; YI, D.; LIIVA, P. Geoscience laser altimeter system (glas) on the icesat mission: on-orbit measurement performance. **Geophysical research letters**, Wiley Online Library, v. 32, n. 21, 2005.

ANDERSON, T. L.; CHARLSON, R. J.; BELLOUIN, N.; BOUCHER, O.; CHIN, M.; CHRISTOPHER, S. A.; HAYWOOD, J.; KAUFMAN, Y. J.; KINNE, S.; OGREN, J. A. et al. An "a-train"strategy for quantifying direct climate forcing by anthropogenic aerosols. **Bulletin of the American Meteorological Society**, American Meteorological Society, v. 86, n. 12, p. 1795–1810, 2005.

ARNOTT, W. P.; DONG, Y. Y.; HALLETT, J.; POELLOT, M. R. Role of small ice crystals in radiative properties of cirrus: A case study, fire ii, november 22, 1991. **Journal of Geophysical Research: Atmospheres**, Wiley Online Library, v. 99, n. D1, p. 1371–1381, 1994.

BOUCHER, O.; LOHMANN, U. The sulfate-ccn-cloud albedo effect. **Tellus B: Chemical and Physical Meteorology**, Taylor & Francis, v. 47, n. 3, p. 281–300, 1995.

CALIPSO, T. **CALIPSO low laser energy technical advisory for data users**. 2018. Disponível em: <https://www-calipso.larc.nasa.gov/resources/calipso_users_guide/advisory/advisory_2018-06-12/CALIPSO_Laser_Energy_Technical_Advisory.pdf>.

CHEPFER, H.; MINNIS, P.; YOUNG, D.; NGUYEN, L.; ARDUINI, R. F. Estimation of cirrus cloud effective ice crystal shapes using visible reflectances from dual-satellite measurements. **Journal of Geophysical Research: Atmospheres**, Wiley Online Library, v. 107, n. D23, p. AAC–21, 2002.

CORDOBA-JABONERO, C.; LOPES, F. J.; LANDULFO, E.; CUEVAS, E.; OCHOA, H.; GIL-OJEDA, M. Diversity on subtropical and polar cirrus clouds properties as derived from both ground-based lidars and calipso/caliop measurements. **Atmospheric Research**, Elsevier, v. 183, p. 151–165, 2017.

CORTI, T.; PETER, T. A simple model for cloud radiative forcing. **Atmospheric Chemistry and Physics**, Copernicus GmbH, v. 9, n. 15, p. 5751–5758, 2009.

CZICZO, D. J.; FROYD, K. D.; HOOSE, C.; JENSEN, E. J.; DIAO, M.; ZONDLO, M. A.; SMITH, J. B.; TWOHY, C. H.; MURPHY, D. M. Clarifying the dominant sources and mechanisms of cirrus cloud formation. **Science**, American Association for the Advancement of Science, v. 340, n. 6138, p. 1320–1324, 2013.

DELANOË, J.; PROTAT, A.; BOUNIOL, D.; HEYMSFIELD, A.; BANSEMER, A.; BROWN, P. The characterization of ice cloud properties from doppler radar measurements. **Journal of applied meteorology and climatology**, American Meteorological Society, v. 46, n. 10, p. 1682–1698, 2007.

FORSTER, P.; STORELVMO, T.; ARMOUR, K.; COLLINS, W.; DUFRESNE, J.-L.; FRAME, D.; LUNT, D.; MAURITSEN, T.; PALMER, M.; WATANABE, M.; WILD, M.; ZHANG, H. The earth's energy budget, climate feedbacks, and climate sensitivity. In: ____. **Climate Change 2021: The Physical Science Basis. Contribution of Working Group I to the Sixth Assessment Report of the Intergovernmental Panel on Climate Change**. Cambridge, United Kingdom and New York, NY, USA: Cambridge University Press, 2021. p. 923–1054.

GOLDFARB, L.; KECKHUT, P.; CHANIN, M.-L.; HAUCHECORNE, A. Cirrus climatological results from lidar measurements at ohp (44 n, 6 e). **Geophysical research letters**, Wiley Online Library, v. 28, n. 9, p. 1687–1690, 2001.

GOUVEIA, D. A.; BARJA, B.; BARBOSA, H. M.; SEIFERT, P.; BAARS, H.; PAULIQUEVIS, T.; ARTAXO, P. Optical and geometrical properties of cirrus clouds in amazonia derived from 1 year of ground-based lidar measurements. **Atmospheric Chemistry and Physics**, Copernicus GmbH, v. 17, n. 5, p. 3619–3636, 2017.

HARTMANN, D. L.; BERRY, S. E. The balanced radiative effect of tropical anvil clouds. **Journal of Geophysical Research: Atmospheres**, Wiley Online Library, v. 122, n. 9, p. 5003–5020, 2017.

HEIRTZLER, J. R. The future of the south atlantic anomaly and implications for radiation damage in space. **Journal of Atmospheric and Solar-Terrestrial Physics**, Elsevier, v. 64, n. 16, p. 1701–1708, 2002.

HEYMSFIELD, A. Cirrus uncinus generating cells and the evolution of cirriform clouds. part i: Aircraft observations of the growth of the ice phase. **Journal of Atmospheric Sciences**, v. 32, n. 4, p. 799–808, 1975.

HEYMSFIELD, A. J. Laboratory and field observations of the growth of columnar and plate crystals from frozen droplets. **Journal of Atmospheric Sciences**, v. 30, n. 8, p. 1650–1656, 1973.

HEYMSFIELD, A. J.; KRÄMER, M.; LUEBKE, A.; BROWN, P.; CZICZO, D. J.; FRANKLIN, C.; LAWSON, P.; LOHMANN, U.; MCFARQUHAR, G.; ULANOWSKI, Z. et al. Cirrus clouds. **Meteorological Monographs**, v. 58, p. 2–1, 2017.

HOSTETLER, C. A.; LIU, Z.; REAGAN, J.; VAUGHAN, M.; WINKER, D.; OSBORN, M.; HUNT, W. H.; POWELL, K. A.; TREPTE, C. Caliop algorithm theoretical basis document - calibration and level 1 data products. **Cloud-Aerosol Lidar Infrared Pathfinder Satellite Observations**, PC-SCI-201 Part 1, p. 1–66, 2006.

HOWARD, L. I. on the modifications of clouds, and on the principles of their production, suspension, and destruction; being the substance of an essay read before the askesian society in the session 1802–3. **The Philosophical Magazine**, Taylor & Francis, v. 17, n. 65, p. 5–11, 1803.

HUNT, W. H.; WINKER, D. M.; VAUGHAN, M. A.; POWELL, K. A.; LUCKER, P. L.; WEIMER, C. Calipso lidar description and performance assessment. **Journal of Atmospheric and Oceanic Technology**, v. 26, n. 7, p. 1214–1228, 2009.

KLETT, J. D. Stable analytical inversion solution for processing lidar returns. **Applied optics**, Optica Publishing Group, v. 20, n. 2, p. 211–220, 1981.

KOVALEV, V. A.; EICHINGER, W. E. **Elastic lidar: theory, practice, and analysis methods**. [S.l.]: John Wiley & Sons, 2004.

KUHN, T.; HEYMSFIELD, A. J. In situ balloon-borne ice particle imaging in high-latitude cirrus. **Pure and Applied Geophysics**, Springer, v. 173, p. 3065–3084, 2016.

LAMARCK, J.-B. d. M. de. **Philosophie zoologique: ou exposition des considérations relatives à l'histoire naturelle des animaux, à la diversité de leur organisation et des facultés qu'ils en obtiennent; aux causes physiques qui maintiennent en eux la vie et donnent lieu aux mouvements qu'ils exécutent; enfin, à celles qui produisent les unes le sentiment, les autres l'intelligence de ceux qui en sont doués. Tome second**. [S.l.]: Librairie F. Savy, 1873. v. 1.

LAWSON, R. P.; BAKER, B.; PILSON, B.; MO, Q. In situ observations of the microphysical properties of wave, cirrus, and anvil clouds. part ii: Cirrus clouds. **Journal of the atmospheric sciences**, v. 63, n. 12, p. 3186–3203, 2006.

LIOU, K.-N. Influence of cirrus clouds on weather and climate processes: A global perspective. **Monthly Weather Review**, v. 114, n. 6, p. 1167–1199, 1986.

LIOU, K.-N. **An introduction to atmospheric radiation**. [S.l.]: Elsevier, 2002. v. 84.

LIU, Z.; OMAR, A. H.; HU, Y.; VAUGHAN, M.; WINKER, D. Caliop algorithm theoretical basis document - part 3: Scene classification algorithms. **Cloud-Aerosol Lidar Infrared Pathfinder Satellite Observations**, PC-SCI-202 Part 3, p. 1–56, 2005.

LOHMANN, U.; LÜÖND, F.; MAHRT, F. **An introduction to clouds: From the microscale to climate**. [S.l.]: Cambridge University Press, 2016.

LYNCH, D. K.; SASSEN, K.; STARR, D. O.; STEPHENS, G. **Cirrus**. [S.l.]: Oxford University Press, 2002.

OU, S.; LIOU, K.-N.; GOOCH, W.; TAKANO, Y. Remote sensing of cirrus cloud parameters using advanced very-high-resolution radiometer 3.7-and 10.9-μm channels. **Applied Optics**, Optical Society of America, v. 32, n. 12, p. 2171–2180, 1993.

PAVÓN-CARRASCO, F. J.; SANTIS, A. D. The south atlantic anomaly: The key for a possible geomagnetic reversal. **Frontiers in Earth Science**, Frontiers Media SA, v. 4, p. 40, 2016.

PROTAT, A.; BOUNIOL, D.; DELANOË, J.; OCONNOR, E.; MAY, P.; PLANA-FATTORI, A.; HASSON, A.; GÖRSDORF, U.; HEYMSFIELD, A. Assessment of cloudsat reflectivity measurements and ice cloud properties using ground-based and airborne cloud radar observations. **Journal of Atmospheric and Oceanic Technology**, v. 26, n. 9, p. 1717–1741, 2009.

ROGERS, R.; YAU, M. A short course in cloud physics. 1989.

ROSAS, J.; BARJA, B. Study of cloud behavior in camagüey (21.4 ºn, 77.8 ºw) using caliop information. **Óptica pura y aplicada**, Sociedad Española de Optica, v. 47, n. 2, p. 115–121, 2014.

SASSEN, K.; CHO, B. S. Subvisual-thin cirrus lidar dataset for satellite verification and climatological research. **Journal of Applied Meteorology and Climatology**, v. 31, n. 11, p. 1275–1285, 1992.

SASSEN, K.; WANG, Z.; LIU, D. Global distribution of cirrus clouds from cloudsat/cloud-aerosol lidar and infrared pathfinder satellite observations (calipso) measurements. **Journal of Geophysical Research: Atmospheres**, Wiley Online Library, v. 113, n. D8, 2008.

SEINFELD, J. H.; PANDIS, S. N. **Atmospheric chemistry and physics: from air pollution to climate change**. [S.l.]: John Wiley & Sons, 2016.

STEPHENS, G. L. Cloud feedbacks in the climate system: A critical review. **Journal of climate**, v. 18, n. 2, p. 237–273, 2005.

STEPHENS, G. L.; VANE, D. G.; BOAIN, R. J.; MACE, G. G.; SASSEN, K.; WANG, Z.; ILLINGWORTH, A. J.; O'CONNOR, E. J.; ROSSOW, W. B.; DURDEN, S. L. et al. The cloudsat mission and the a-train: A new dimension of space-based observations of clouds and precipitation. **Bulletin of the American Meteorological Society**, American Meteorological Society, v. 83, n. 12, p. 1771–1790, 2002.

VAUGHAN, M.; WINKER, D.; POWELL, K. A. Caliop algorithm theoretical basis document - part 2: Feature detection and layer properties algorithms. **Cloud-Aerosol Lidar Infrared Pathfinder Satellite Observations**, PC-SCI-202 Part 2, p. 1–87, 2005.

VAUGHAN, M. A.; POWELL, K. A.; WINKER, D. M.; HOSTETLER, C. A.; KUEHN, R. E.; HUNT, W. H.; GETZEWICH, B. J.; YOUNG, S. A.; LIU, Z.; MCGILL, M. J. Fully automated detection of cloud and aerosol layers in the calipso lidar measurements. **Journal of Atmospheric and Oceanic Technology**, v. 26, n. 10, p. 2034–2050, 2009.

WEITKAMP, C. **Lidar: range-resolved optical remote sensing of the atmosphere**. [S.l.]: Springer Science & Business, 2006. v. 102.

WINKER, D.; PELON, J.; JR, J. C.; ACKERMAN, S.; CHARLSON, R.; COLARCO, P.; FLAMANT, P.; FU, Q.; HOFF, R.; KITTAKA, C. et al. The calipso mission: A global 3d view of aerosols and clouds. **Bulletin of the American Meteorological Society**, American Meteorological Society, v. 91, n. 9, p. 1211–1230, 2010.

WINKER, D. M. Accounting for multiple scattering in retrievals from space lidar. In: SPIE. **12th International Workshop on Lidar Multiple Scattering Experiments**. [S.l.], 2003. v. 5059, p. 128–139.

WINKER, D. M.; COUCH, R. H.; MCCORMICK, M. An overview of lite: Nasa's lidar in-space technology experiment. **Proceedings of the IEEE**, IEEE, v. 84, n. 2, p. 164–180, 1996.

WINKER, D. M.; HUNT, W. H.; MCGILL, M. J. Initial performance assessment of caliop. **Geophysical Research Letters**, Wiley Online Library, v. 34, n. 19, 2007.

WINKER, D. M.; VAUGHAN, M. A.; OMAR, A.; HU, Y.; POWELL, K. A.; LIU, Z.; HUNT, W. H.; YOUNG, S. A. Overview of the calipso mission and caliop data processing algorithms. **Journal of Atmospheric and Oceanic Technology**, v. 26, n. 11, p. 2310–2323, 2009.

INSTITUTO DE PESQUISAS ENERGÉTICAS E NUCLEARES
Diretoria de Pesquisa, Desenvolvimento e Ensino
Av. Prof. Lineu Prestes, 2242 – Cidade Universitária CEP: 05508-000
Fone/Fax(0XX11) 3133-8908
SÃO PAULO – São Paulo – Brasil
http://www.ipen.br

O IPEN é uma Autarquia vinculada à Secretaria de Desenvolvimento, associada à Universidade de São Paulo e gerida técnica e administrativamente pela Comissão Nacional de Energia Nuclear, órgão do Ministério da Ciência, Tecnologia, Inovações e Comunicações.